Carbon cycle, vegetation, and climate dynamics in the Holocene: Experiments with the CLIMBER-2 model

Victor Brovkin, Jørgen Bendtsen, Martin Claussen,[1] Andrey Ganopolski, Claudia Kubatzki, Vladimir Petoukhov, and Andrei Andreev

Potsdam-Institut für Klimafolgenforschung, Potsdam, Germany

[1]   Multiple proxy data reveal that the early to middle Holocene (ca. 8–6 kyr B.P.) was warmer than the preindustrial period in most regions of the Northern Hemisphere. This warming is presumably explained by the higher summer insolation in the Northern Hemisphere, owing to changes in the orbital parameters. Subsequent cooling in the late Holocene was accompanied by significant changes in vegetation cover and an increase in atmospheric CO_2 concentration. The essential question is whether it is possible to explain these changes in a consistent way, accounting for the orbital parameters as the main external forcing for the climate system. We investigate this problem using the computationally efficient model of climate system, CLIMBER-2, which includes models for oceanic and terrestrial biogeochemistry. We found that changes in climate and vegetation cover in the northern subtropical and circumpolar regions can be attributed to the changes in the orbital forcing. Explanation of the atmospheric CO_2 record requires an additional assumption of excessive $CaCO_3$ sedimentation in the ocean. The modeled decrease in the carbonate ion concentration in the deep ocean is similar to that inferred from $CaCO_3$ sediment data [*Broecker et al.*, 1999]. For 8 kyr B.P., the model estimates the terrestrial carbon pool ca. 90 Pg higher than its preindustrial value. Simulated atmospheric $\delta^{13}C$ declines during the course of the Holocene, similar to $\delta^{13}C$ data from the Taylor Dome ice core [*Indermühle et al.*, 1999]. Amplitude of simulated changes in $\delta^{13}C$ is smaller than in the data, while a difference between the model and the data is comparable with the range of data uncertainty.   *INDEX TERMS:* 0330 Atmospheric Composition and Structure: Geochemical cycles; 0315 Atmospheric Composition and Structure: Biosphere/atmosphere interactions; 1620 Global Change: Climate dynamics (3309); 4806 Oceanography: Biological and Chemical: Carbon cycling

1.   Introduction

[2]   Ice core based reconstructions of past climate changes [*Jouzel et al.*, 1987; *Grootes et al.*, 1993; *Blunier and Brook*, 2001] estimate the onset of the current interglacial epoch, the Holocene, to ca. 11.5 thousand years before present (kyr B.P.). Multiple proxy data (pollen data, macrofossils) reveal that the summer climate in the Northern Hemisphere was warmer in the early to middle Holocene (ca. 8–6 kyr B.P.) relative to the preindustrial climate [*Velichko et al.*, 1997; *Prentice et al.*, 2000]. This warming has been explained by variations in orbital forcing: the Northern Hemisphere received more solar radiation in the boreal summer during the mid-Holocene than at present [*Berger*, 1996]. The

orbital forcing hypothesis for the mid-Holocene has been successfully tested with climate models of different complexity [*Kutzbach et al.*, 1996; *Hewitt and Mitchell*, 1996; *Pollard et al.*, 1998; *Ganopolski et al.*, 1998; *Crucifix et al.*, 2002].

[3]   Expanded vegetation cover in the northern circumpolar region and in the northern subtropics suggests that the amount of carbon stored in the vegetation and soils during the mid-Holocene was higher than at preindustrial [e.g., *Adams et al.*, 1990]. Moreover, ice core data from the Vostok [*Barnola et al.*, 1993] and the Taylor Dome [*Indermühle et al.*, 1999] show that the atmospheric CO_2 concentration during 9–8 kyr B.P. was about 20 ppmv lower than the preindustrial level. Analyzing the $\delta^{13}C$ record from the Taylor Dome, *Indermühle et al.* [1999] suggested that an increase in the atmospheric CO_2 concentration during the course of the Holocene was mainly caused by the decay of terrestrial carbon accumulated in the early Holocene. Alternatively, *Broecker et al.* [1999] suggested that the increase

---

[1]Also at Institut für Meteorologie, Freie Universität Berlin, Berlin, Germany.

Table 1. Summary of Equilibrium Simulations[a]

Acronym	Simulation purpose	Time slice	Atm. CO_2 (ppmv)	$\delta^{13}C_{ATM}$ (‰)	Changes in $CO_3^=$[b] (μeq/kg)	Mean ocean ALK (μeq/kg)
		Reference				
AOVC-0K	Reference for 0K	Preindustrial[c]	280	−6.5	–	2373
AOVC-8K	Reference climate for 8K	8000 years B.P.[d]	260	−6.4[e]	5	2373
		Carbon Cycle Sensitivity				
AOVC-0K-co2	Sensitivity to atm. CO_2	Preindustrial	280/260[f]	–	–	2373
AOVC-8K-clm	Sensitivity to climate	8000 years B.P.	260/280[f]	–	–	2373
		Initial Conditions for Transient Simulations				
AOVC-8K-H	Initial conditions for AOVC-T	8000 years B.P.	260	−6.4	8	2406
AOVC-8K-O	Initial conditions for AOVC-T-O	8000 years B.P.	260	−6.4	9.5	2421

[a] The simulations are done for 10,000 years with prescribed boundary conditions (insolation, CO_2, ALK).
[b] Changes in pressure-corrected carbonate ion concentration in deep tropical ocean in comparison with AOVC-0K.
[c] The simulation corresponds to present-day climate and preindustrial carbon cycle.
[d] Insolation changes are prescribed in accordance with the work of *Berger* [1996].
[e] $\delta^{13}C_{ATM}$ is prescribed following a spline estimate for the Taylor Dome data at 8000 years B.P. (see *Indermühle et al.* [1999] Figure 2).
[f] Atmospheric CO_2 concentration for climate/carbon cycle models.

in the atmospheric CO_2 concentration during the Holocene can be explained by accounting for a carbonate compensation mechanism in the ocean, which operates on a timescale of the order of 5000 years. Presumably, CO_2 release from the ocean during glacial–interglacial transition [*Archer et al.*, 2000] led to an increase in the carbonate ion concentration in the deep ocean and a deepening of saturation horizon for calcite. The oceanic carbonate system had reacted by excessive accumulation of $CaCO_3$ sediments and restoring of the carbonate ion concentration in the deep ocean. As a result, total ocean alkalinity declined, CO_2 solubility decreased, and atmospheric CO_2 concentration increased. The latter hypothesis is supported by analysis of carbonate sediments in the deep tropical ocean and broad-scale evidence of excessive accumulation of $CaCO_3$ in the ocean during the Holocene [*Milliman*, 1993].

[4] These hypotheses can be tested by using of prognostic models of the global carbon cycle. The essential task is to explain the changes in carbon cycle during the Holocene in a way consistent with climate and vegetation changes, assuming that variations in the orbital parameters are the only external forcing. We investigate this problem with the climate system model CLIMBER-2 that includes dynamic atmosphere, ocean, and vegetation models as well as oceanic biogeochemistry model.

[5] The paper is organized in the following way. First we describe the terrestrial and oceanic biogeochemical components and present results for the preindustrial simulation AOVC-0K (Atmosphere–Ocean–Vegetation–Carbon simulation with boundary conditions at 0 kyr B.P.; see Table 1 for experiment acronyms). Then we discuss equilibrium simulations for 8 kyr B.P. Finally, we present results of

transient simulations from 8 kyr B.P. till the preindustrial (see Table 2) and compare them with available proxy.

2. Model Description and Performance for Present-Day Climate

[6] CLIMBER-2 is a climate system model of intermediate complexity [*Petoukhov et al.*, 2000]. It includes a 2.5-dimensional dynamical-statistical atmosphere model with a coarse spatial resolution of $10°$ in latitude and $51°$ in longitude, a multibasin, zonally averaged ocean model, including a sea ice model, which operates with latitudinal resolution of $2.5°$ and a terrestrial vegetation model. Results of CLIMBER-2 compare favorably with data of the present-day climate [*Petoukhov et al.*, 2000], with paleoclimatic reconstructions [*Ganopolski et al.*, 1998; *Claussen et al.*, 1999a; *Kubatzki et al.*, 2001] and with results from sensitivity experiments undertaken with comprehensive models [*Ganopolski et al.*, 2001].

2.1. Atmosphere–Vegetation Coupling

[7] In CLIMBER-2, the vegetation model interacts with the atmospheric model. At the end of the simulation year, output of the atmospheric model (temperature and precipitation fields) is used for simulating vegetation cover and the terrestrial carbon cycle. In turn, the vegetation cover and the maximum of leaf area index (LAI) are accounted for in calculating the surface albedo, roughness, and evapotranspiration during the following simulation year. The land surface component in CLIMBER-2 has daily time step; it treats land as a fractional composition of simple land surface types (trees, grass, desert, and ice). The description of land

Table 2. Summary of Transient Simulations From 8 kyr B.P. to Preindustrial

Acronym	Simulation purpose	Initial/final atm. CO_2[a] (ppmv)	Initial/final $\delta^{13}C_{ATM}$ (‰)	Initial/final mean ocean ALK (μeq/kg)	$CaCO_3$ sedimentation (PgC)
AOVC-T	Baseline transient	260/280	−6.4/−6.45	2406/2373	270
AOVC-T-O	"Ocean only" carbon source	260/280	−6.4/−6.4	2421/2373	390

[a] Atmospheric CO_2 is interactive with terrestrial and oceanic carbon cycle. Total carbon amount in the system (including ocean sediments) is conserved.

surface processes is based on the biosphere–atmosphere transfer scheme by *Dickinson et al.* [1993].

2.2. Terrestrial Biosphere

[8] The model for the terrestrial biosphere VECODE [*Cramer et al.*, 2001; V. Brovkin et al., Vegetation Continuous Description Model (VECODE): Technical report, PIK Report, Potsdam-Institut für Klimafolgenforschung, Germany, in preparation, 2002] was designed specifically with the purpose of interactive coupling with a coarse resolution atmospheric model for long-term simulations. It is a reduced-form dynamic global vegetation model (DGVM), which simulates changes in vegetation structure and terrestrial carbon pools on a timescale from decades to millennia. Plant functional types (PFTs) [e.g., *Prentice et al.*, 1992; *Chapin et al.*, 1996] for PFT conception) are used to describe vegetation cover (section 2.2.1). For any given climate, there is a unique stable composition of PFTs corresponding to the climate (in this context, we refer to climate as long-term averaged atmospheric fields). If climate changes, then the vegetation model simulates the transition from the equilibrium for the previous climate to a new equilibrium with the new climate (section 2.2.3). The timescale of this transition is determined from the carbon cycle model (section 2.2.2).

2.2.1. Bioclimatic Classification

[9] A fractional bioclimatic classification [*Brovkin et al.*, 1997] is developed in order to adapt discrete bioclimatic classifications (e.g., Life Zones by *Holdridge* [1947] or BIOME by *Prentice et al.* [1992]) for coarse resolution climate models. Two basic PFTs are used: trees and grasses. The sum of tree fraction, f, and grass fraction, g, is equal to vegetation fraction, v; the rest is desert fraction, $d = 1 - v$. These transient fractions are different from equilibrium fractions (vegetation in equilibrium with climate), denoted by $\hat{f}$, $\hat{v}$. Semiempirical parameterizations for $\hat{f}$(A11) and $\hat{v}$(A12)–(A14) are based on regularities of distribution of forest and desert in climatic space [*Lieth*, 1975] which have ecophysiological basis [*Woodward*, 1987]. Vegetation map by *Olson et al.* [1985] and updated version (Cramer, personal communication) of climate data set by *Leemans and Cramer* [1991] were used in the validation procedure.

[10] CLIMBER-2 is able to simulate the basic global patterns of the present-day potential vegetation cover: A boreal forest belt, tropical forests (see Figure 1a), subtropical deserts in Africa and Eurasia (Figure 1c). Grasses occupy a significant part of high latitude regions as well as subtropical areas (Figure 1b). In midlatitudes in northern America, the model overestimates the tree fraction due to the coarse model resolution: the strong W-E gradient in precipitation is not represented by the mean value across the continent.

2.2.2. Carbon Cycle

[11] Carbon in vegetation is aggregated into two compartments: a "fast" pool of green biomass (leaves), C_Φ^1, and a "slow" pool of structural biomass (stems, roots), C_Φ^2. Dead organic matter is described by two pools: a "fast" compartment (woody residues), C_Φ^3, and a "slow" compartment (humus), C_Φ^4. Variables C_Φ^i are simulated separately for trees and grass. The dynamics of the carbon pools are integrated with an annual time step (A1)–(A4). These equations are
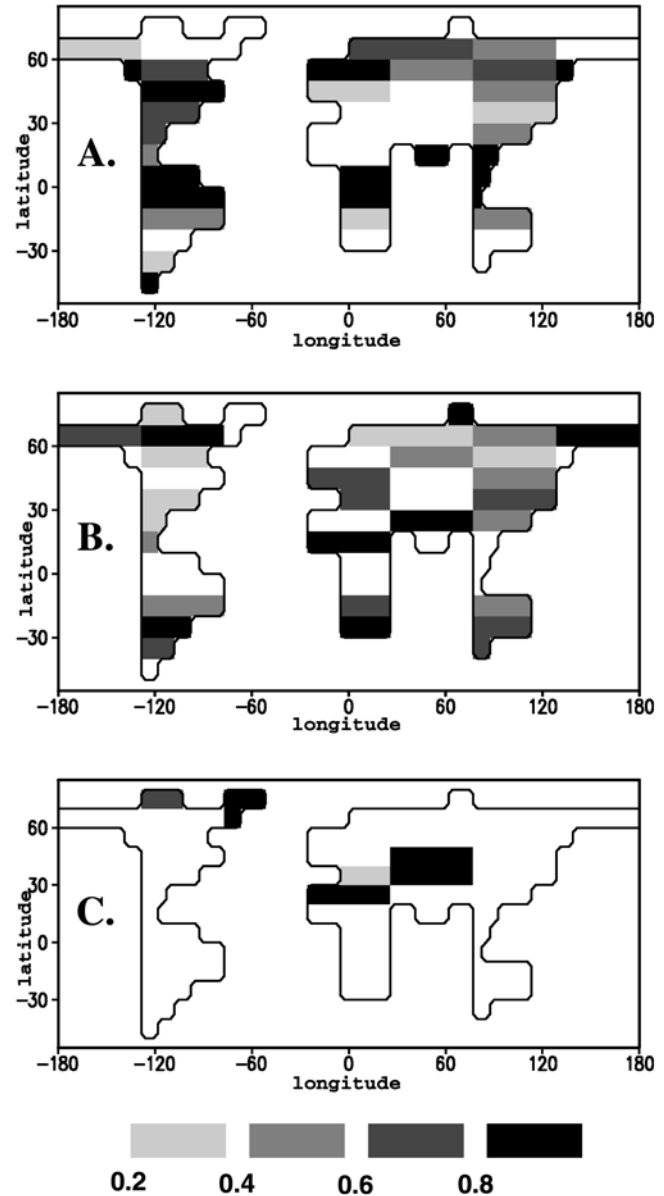

Figure 1. Vegetation cover in CLIMBER-2. (a) Tree fraction. (b) Grass fraction. (c) Desert fraction.

written in general form for ^{12}C and ^{13}C. Net primary productivity (NPP), Π, is simulated on an annual basis following the semiempirical parameterization (A5) by *Lieth* [1975] which is often used for first-guess estimations on a global scale [*Post et al.*, 1997]. (A5) compares favorably with bulk measurements for NPP for present-day climate everywhere except in the dry subtropical regions where it overestimates productivity. In these regions NPP is corrected by accounting for the vegetation fraction (A12) as NPP averaged over the grid cell is equal to $\Pi \cdot v$. Dependence of NPP on the atmospheric CO_2 concentration, C_{atm}, is taken into account by the biotic growth factor in a logarithmic form (A5) [*den Elzen et al.*, 1995].

[12] NPP allocation between green and structural biomass is estimated as a function of NPP, with increased allocation

Table 3. Variables and Parameters of the Carbon Cycle Model[a]

Variable, parameter	Term	Value	Units
	Land		
Tree fraction	f	var.	
Equilibrium tree fraction	f^*	var.	
Vegetation fraction	v	var.	
Equilibrium vegetation fraction	v^*	var.	
Grass fraction	g	var.	
Relative fraction of C_3-type grass	g_3	var.	
Carbon storage	C_Φ^i	var.	kgC m^{-2}
Carbon lifetime	τ_Φ^i	var.	years
NPP	Π	var.	kgC m^{-2} yr^{-1}
NPP allocation factor	k_Φ^1	var.	
Parameters of carbon allocation	$k_\Phi^i, i \geq 2$	const.	
Parameters of allocation dependences	$n_\Phi^i, m_\Phi^{i,j}$	const.	
Mean annual surface air temperature	T_a	var.	°C
Growing degree days above 0	G_0	var.	degree days
Annual mean precipitation	P_r	var.	mm yr^{-1}
Bioclimatic parameters	$a, a_{for}, a_{des},$	const.	
	b, b_2, c	const.	
Maximum tree fraction	f_{max}	0.95	
Minimum precipitation for vegetation	P_r^{min}	var.	mm yr^{-1}
Threshold in v timescale	v_{min}	0.1	
Minimum GDD0 for trees	G_{min}	800	degree days
Atmospheric CO_2 concentration	C_{atm}	var.	ppmv
Reference atmospheric CO_2 concentration	C_{atm}^0	280	ppmv
Maximum NPP for C_{atm}^0	Π_{max}	1.4	kgC m^{-2} yr^{-1}
NPP regressional parameters	v_i	const.	
Factor of NPP dependence on C_a	β	0.2	
Carbon isotopic fractionation factor during photosynthesis	α_Φ^*	var.	
Atmospheric carbon isotopic ratio	R_Φ^*	var.	
^{13}C fractionation factor for C_3 plants	α_3^{13}	0.982	
^{13}C fractionation factor for C_4 plants	α_4^{13}	0.995	
	Ocean		
Tracer source minus sink due to cycle of organic matter	$J_{org}(\Gamma)$	var.	
Tracer source minus sink due to cycle of $CaCO_3$	$J_{car}(\Gamma)$	var.	
DIC concentration	C_{dic}	var.	μmol kg^{-1}
DOC concentration	C_{doc}^i	var.	μmol kg^{-1}
PO_4 concentration	P	var.	μmol kg^{-1}
O_2 concentration	O_2	var.	μmol kg^{-1}
Alkalinity concentration	ALK	var.	μeq kg^{-1}
Phytoplankton concentration	C_p	var.	μmol kg^{-1}
Zooplankton concentration	C_z	var.	μmol kg^{-1}
Net primary productivity	Π	var.	μmol kg^{-1} s^{-1}
Grazing	G	var.	μmol kg^{-1} s^{-1}
Sea surface temperature	T	var.	°C
Incoming surface shortwave radiation	L	var.	W m^{-2}
NPP dependence on T and L	$r(T,L)$	var.	
Grazing dependence on T	$g_T(T)$	var.	
Half-saturation constant for nutrient uptake	P^0	0.016	μmol P kg^{-1}
Half-saturation constant for phytoplankton ingestion	C_p^0	3.5	μmol C kg^{-1}
Egestion as fecal pellets from herbivores	$1 - \epsilon_{her}$	0.1	
Egestion as fecal pellets from carnivores	$1 - \epsilon_{can}$	0.95	
Specific mortality rate for phytozooplankton	d_p, d_z	0.008	day^{-1}
Exudation rate of DOC	γ_p	0.03	day^{-1}
Excretion rate of DOC	γ_z	0.06	day^{-1}
Assimilation efficiency	ζ	0.6	
Shifted C_p, C_z	C_p', C_z'	var.	μmol kg^{-1}
New production flux	$E(z)$	var.	μmol kg^{-1} s^{-1}
Depth of euphotic layer	z_{eup}	100	m
DOC remineralization	D^i	var.	μmol kg^{-1} s^{-1}
POC remineralization	F_{dic}	var.	μmol kg^{-1} s^{-1}
DOC source	F_{doc}^i	var.	μmol kg^{-1} s^{-1}
$CaCO_3$ source	F_{car}	var.	μmol kg^{-1} s^{-1}
DOC/P ratio	η_{doc}	106	
N/P ratio	η_N	16	
DIC/P ratio for $E(z)$	$\eta_{dic}(z)$	Table 4	
O_2/P ratio for remineralization of $E(z)$	$\eta_{O_2}(z)$	Table 4	
DOC allocation factor	l_f^s	0.1	
Remineralization allocation	$\theta(z)$	var.	
Remineralization parameter	a_θ	−0.858	
Carbonate allocation	$\kappa(z)$	var.	m

Table 3. (continued)

Variable, parameter	Term	Value	Units
Mean dissolution depth	d_κ	3000	m
Rain ratio	R_r	0.1	
DIC carbon isotopic ratio	$R*$	var.	
^{13}C fractionation factor for photosynthesis	α_{org}^{13}	var.	
Decay constant for ^{14}C	λ^{14}	3.84e^{-12}	s^{-1}

[a] Functions $r(T, L)$ and $g_T(T)$ are given by *Six and Maier-Reimer* [1996, equations (1)–(4)]. Grazing rate g_0 of *Six and Maier-Reimer* [1996, equation (4)] is increased to 1.0. Parameter ζ corresponds to *zinges* [*Six and Maier-Reimer*, 1996]. Parameter $1 - \epsilon_{her}$ is chosen between 0 and 0.2 (K. Six, personal communication).

to C_Φ^2 relative to C_Φ^1 as NPP increases (A6). For calibration of this function, we used an empirical data set of NPP and carbon storage from about 500 sites in the northern Eurasia, collected by *Bazilevich* [1993]. The same data were used for calibrating parameterizations for the turnover time of biomass τ_Φ^i, $i = 1, 2$, which is assumed to be a function of NPP (A7). The turnover time of soil carbon τ_Φ^i, $i = 3, 4$, is a function of the mean annual temperature following the approach by *Schimel et al.* [1994]. The annual maximum of LAI is assumed to be proportional to the green biomass.

[13] For simulation of the global ^{13}C budget the grass fraction is diagnostically separated into fractions of C_3 and C_4 types, g_3 and $g - g_3$ correspondingly, applying a coldest month temperature threshold similar to the work of *Haxeltine and Prentice* [1996, equation (A17)]. The only simulated difference between C_3 and C_4 grasses is ^{13}C fractionation (see Table 3). Results for the terrestrial carbon cycle from the AOVC-0K simulation are presented in the Figures 2 and 3. For potential vegetation (without historical deforestation), the model estimates global NPP of 56 PgC yr^{-1} and biomass and soil carbon of 850 and 1080 PgC, respectively. Most of the carbon (ca. 85%) is allocated to the C_3 photosynthesis pathway and the remaining carbon (15%) to the C_4 pathway. The globally averaged δ^{13}C fractionation factor for terrestrial biosphere is 0.984.

2.2.3. Vegetation Dynamics

[14] To account for the subgrid-scale processes of vegetation succession, we apply linear equations (A8) and (A9) for simulating the dynamics of the PFT fractions. The model implies that the vegetation cover reacts to any climate change with a relaxation toward a new equilibrium with a timescale determined by the turnover time of the structural biomass. For instance, if the climate becomes more wet and the equilibrium fraction of trees increases, then the trees become more successful in competing with grasses and occupy an additional fraction of land within the large grid cell with a timescale of tree growth. In vicinity of an equilibrium, (A8) is a linearized version of the evolutionary model for vegetation dynamics [*Svirezhev*, 1999] which accounts for competition between trees and grasses in the idealized form. With respect to the dynamics of the northern tree line under CO_2-induced climate change, VECODE shows similar performance to other dynamic global vegetation models [*Cramer et al.*, 2001].

2.3. Ocean Biogeochemistry

[15] We account for the biogenic production and the subsequent remineralization of organic and inorganic matter (calcium carbonate shells) in the ocean. Sources from riverborne material and aeolian dust, sinks due to sedimen-
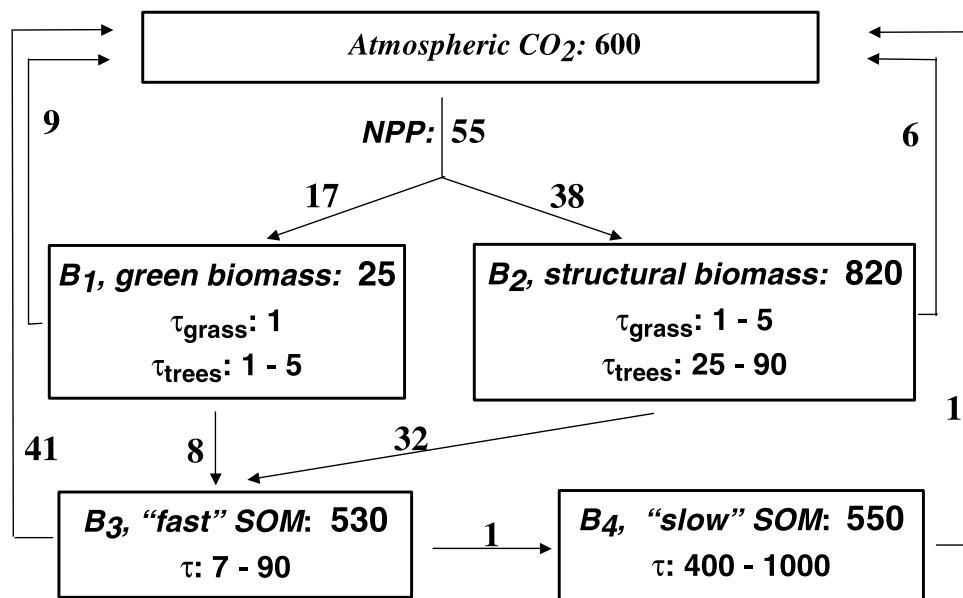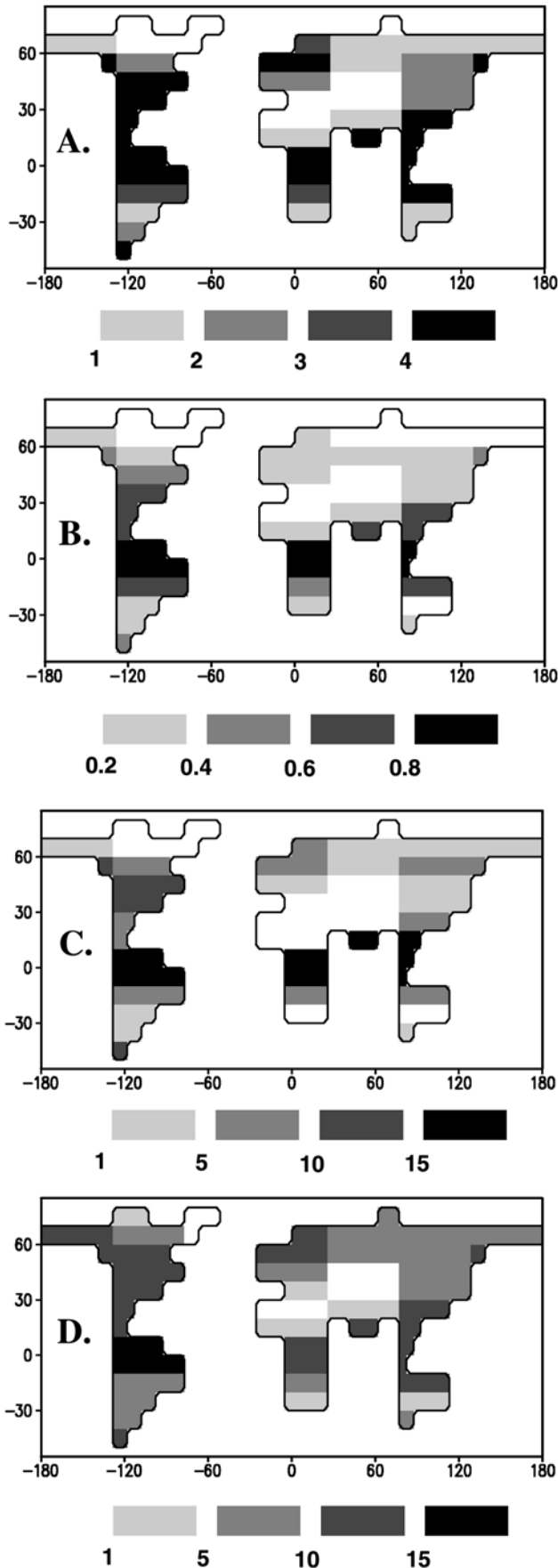

Figure 2. Scheme of the terrestrial carbon cycle in CLIMBER-2 (AOVC-0K). Units are Pg for carbon storages and Pg yr^{-1} for carbon fluxes.

tation are neglected. The biogeochemical tracers (Γ) considered in the model are phosphate (PO_4), oxygen (O_2), alkalinity (ALK), dissolved inorganic carbon (DIC, concentration denoted as C_{dic}), two types of dissolved organic carbon (DOC, concentration denoted as C_{doc}^f and C_{doc}^s for fast and slow pools, respectively), as well as the carbon isotopes (^{13}C and ^{14}C) for DIC and DOC. The conservation equation (B1) is solved for every tracer Γ, where $A_d(\Gamma)$ is advective, diffusive, and convective transports and $J_{org}(\Gamma)$ and $J_{car}(\Gamma)$ are internal sources and sinks associated with organic and inorganic ($CaCO_3$) carbon, respectively. Equations for DIC and DOC are written in general form for ^{12}C and [13]C. For radiocarbon $J(\Gamma)$ includes the third term, $J_r(\Gamma)$, associated with radiocarbon decay.

[16] The global mean phosphate and alkalinity values of 2.08 and 2373 μeq kg^{-1}, respectively, were obtained from the WOA94 [*Conkright et al.*, 1994], GEOSECS and the TTO data sets. These global mean values are in accordance with previous used values [e.g., *Shaffer*, 1996; *Bacastow and Maier-Reimer*, 1990].

[17] At the sea surface, DIC and O_2 are exchanged with the atmosphere. The concentration of O_2 in the upper ocean layer is assumed to be saturated. For CO_2 and its isotopes the surface exchange is determined from the difference in the partial pressure of CO_2 in the air and in the surface water with the gas exchange coefficient of 0.06 mol m^{-2} yr^{-1} μatm^{-1} derived by balancing the air–sea gas exchange of ^{14}C with the total decay of ^{14}C in the ocean [*Siegenthaler*, 1986]. The pCO_2 in the surface water is calculated from surface temperature, salinity, DIC, and ALK in accordance with the work of *Millero* [1995]. *Marchal et al.*'s [1998] equations (30)–(34) are used to account for the temperature dependence of ^{13}C fractionation factor on DIC components. Biological fractionation factor, α_{org}^{13}, depends on CO_2(aq) in accordance with the work of *Rau et al.* [1989].

[18] Biological processes in the euphotic zone (the upper 100 m in the model) are explicitly resolved using the model for plankton dynamics by *Six and Maier-Reimer*, [1996] (see (B2)–(B18)). This model is modified to account for a slow DOC pool with timescale of 40 years. Globally averaged concentration of the slow DOC is about 5 μmol kg^{-1}; a small fraction (10%) of the detritus produced in the photic layer is allocated into this pool (B17).

[19] It is widely assumed that the availability of nitrate and, is some places, of iron governs biological productivity. However, the utilization of nitrogen is accompanied by phosphate uptake, and stoichiometric ratio of nitrogen to phosphorus in biological production is almost constant. We follow a simplified approach by *Six and Maier-Reimer* [1996] that the phytoplankton productivity is limited by phosphate. Remineralization of particulate organic carbon (POC) and dissolution of $CaCO_3$ in the aphotic layer are functions of depth (B19)–(B22) following the approach by

Figure 3. (opposite) Map of vegetation characteristics in CLIMBER-2 (AOVC-0K). (a) Maximum LAI. (b) NPP (kgC m^{-2}). (c) Total biomass (kgC m^{-2}). (d) Total soil carbon (kgC m^{-2}).
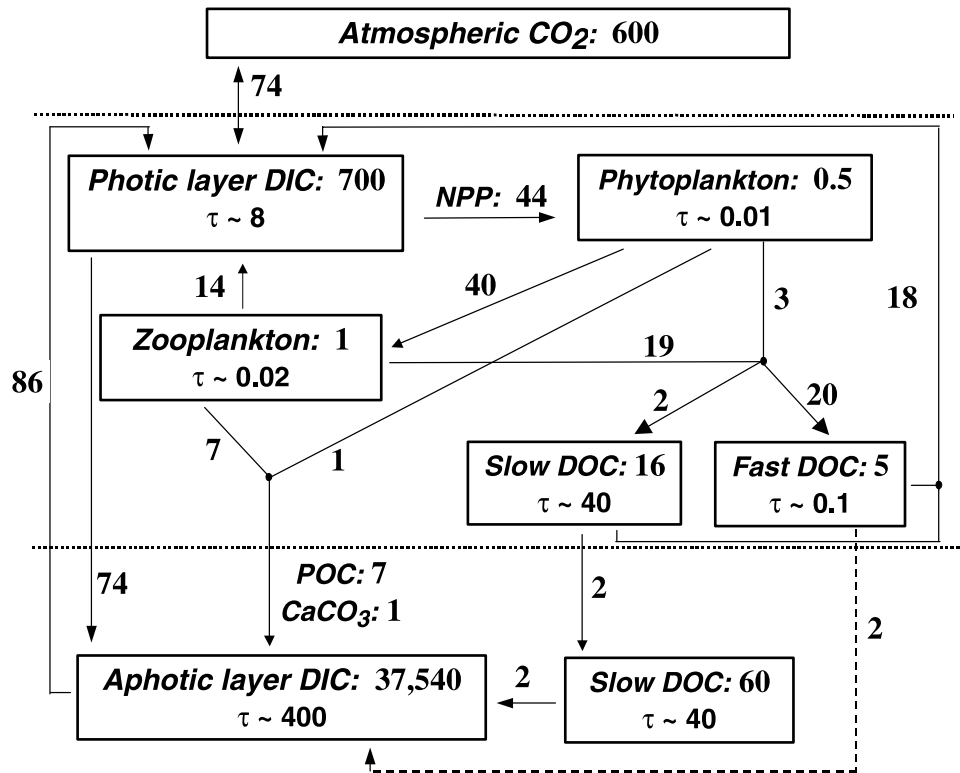
Figure 4. Scheme of the oceanic carbon cycle in CLIMBER-2 (AOVC-0K). Units are Pg for carbon storages and Pg yr^{-1} for carbon fluxes. Dotted lines are for boundaries of the photic surface layer. Dashed arrow represents fast DOC, which is physically transported and remineralized in the deep ocean.

Yamanaka and Tajika [1996] and *Martin et al.* [1987]. The mass balance for POC and $CaCO_3$ is satisfied by remineralization of the flux reaching the ocean floor in the deepest model cells in accordance with approach by *Marchal et al.* [1998]. During remineralization of organic matter we assume fractionation between nutrients and carbon such that C/P ratio, $\eta_{dic}(z)$, increases nonlinearly from the traditional Redfield value (106) at the surface to 125 below 2000 m depth [*Shaffer et al.*, 1999]. The O_2/P ratio, $\eta_{O_2}(z)$, changes almost linear from -138 at the surface to -170 below 2500 m depth (B24) in accordance with the work of *Shaffer et al.*, [1999]. The mass balance in the vertical column is conserved by decreasing values for $\eta_{dic}(z)$ and $\eta_{O_2}(z)$ in the depth interval from 100 to 500 m to ca. 103:1 and 133:1 for C/P and O_2/P, respectively.

[20] The results for AOVC-0K are shown in Figure 4. Global oceanic NPP is about 44 PgC yr^{-1}, POC is 7.2 PgC yr^{-1}, $CaCO_3$ flux is ca. 0.7 PgC yr^{-1}. The advective and diffusive transport of DOC from the surface layer is 2 PgC yr^{-1} for the labile DOC pool, which has a half-life of less than 1 year, and about 2 PgC yr^{-1} for the slowly decomposing DOC pool.

[21] Distributions of PO_4, DIC, and ALK within three ocean basins are presented in Figure 5. These distributions are determined by ocean circulation fields provided by the circulation model as well as by the biological processes simulated by the model for marine biota. In general, the model tends to overestimate near-surface concentration of phosphate in the tropical regions (Figures 4a and 4b).

Introducing of slow pool of DOC within the model reduces the nutrient trapping in agreement with the work of *Marchal et al.* [1998]. However, the usefulness of this approach is limited because a high level of nutrients transport with slow DOC leads to unrealistically diffusive spatial structure of the tracer fields. In the intermediate to deep ocean, distributions of phosphate, DIC (Figures 4c and 4d) and ALK (see Figures 4e and 4f) are in good agreement with the data. Distribution of O_2 (not shown) reflects the distribution of PO_4; the minimum of oxygen concentration (10–50 µmol kg^{-1}) is reached below the euphotic layer in the tropical Pacific and Indian.

[22] A scheme for global carbon cycle for (AOVC-0K) is presented in Figure 6. The oceanic and terrestrial carbon storages are 38,320 and 1930 PgC, respectively. Although oceanic storage of DIC is much larger than terrestrial carbon pool, oceanic and terrestrial net primary productivities are similar (44 and 55 PgC yr^{-1}, respectively).

3. Carbon Cycle Simulation for the Holocene
3.1. Equilibrium Simulations for 8 kyr B.P.

[23] We choose 8 kyr B.P. as a time for initial conditions because of features of atmospheric CO_2 record inferred from the Taylor Dome ice core [*Indermühle et al.*, 1999]. This period was a turning point in atmospheric CO_2 dynamics: after a gradual decline to 260 ppmv the CO_2 concentration started to increase again. The atmospheric CO_2 concentration was nearly constant during 8800–8000
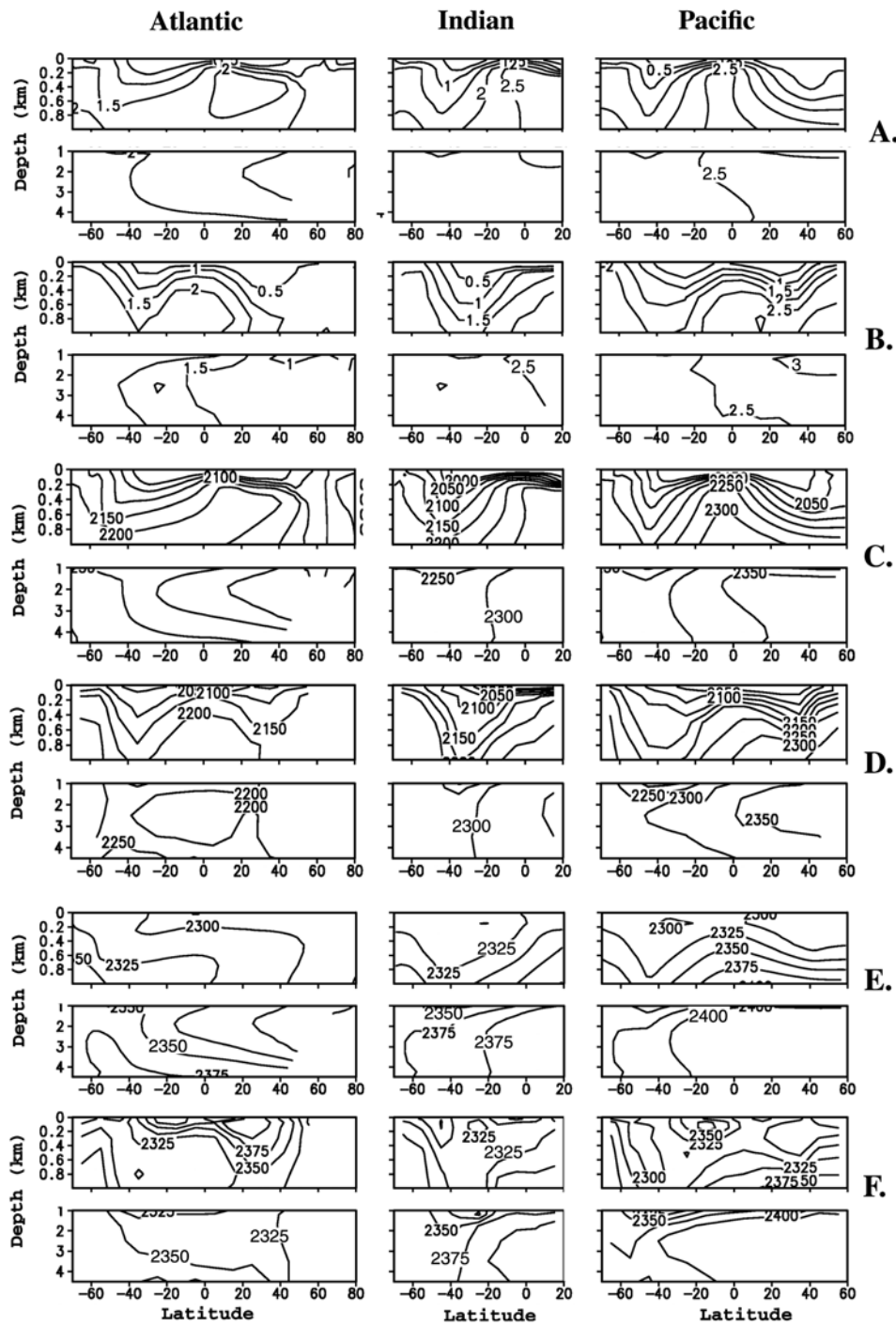
Figure 5. Distribution of the biogeochemical tracers (PO$_4$, DIC, and ALK) in the ocean basins (AOVC-0K). (a) Model PO$_4$ concentration (μmol kg^{-1}). (c) Model DIC concentration (μmol kg^{-1}). (e) Model alkalinity (μeq kg^{-1}). (b), (d), and (f) GEOSECS data zonally averaged and interpolated onto the model grid for PO$_4$, DIC, and ALK, correspondingly.

years BP, such that the processes with timescales of up to several hundred years were in equilibrium with atmospheric CO$_2$ concentration around 8 kyr B.P.

[24] In the equilibrium simulation for the Holocene (AOVC-8K, see Table 1) the atmospheric CO$_2$ concentration is fixed to 260 ppmv. For atmospheric δ^{13}C we use a value −6.4‰ (following spline estimate for the Taylor Dome data at 8 kyr B.P., see the work of *Indermühle et al.* [1999, Figure 2]). Orbital forcing is prescribed following *Berger* [1996]. Sea level and inland ice distribution are the same as in (AOVC-0K). With these boundary conditions and initial conditions taken from (AOVC-0K), we simulate 10,000
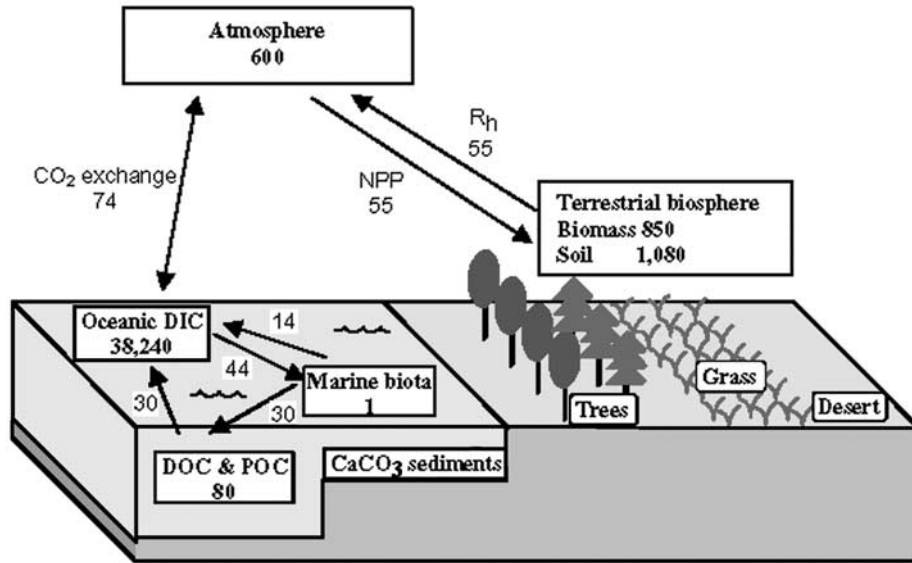
Figure 6. Scheme of the global carbon cycle in CLIMBER-2, preindustrial steady state. Units are Pg for carbon storages and Pg yr^{-1} for carbon fluxes. See color version of this figure at back of this issue.

years of the coupled atmosphere, ocean, vegetation and biogeochemistry modules until equilibrium is approached.

3.1.1. Changes in Climate

[25] Spatial distribution of temperature and precipitation changes (AOVC-8K minus AOVC-0K) is presented in Figure 7. System response is determined by seasonal asymmetry in orbital forcing, lowered atmospheric CO_2 concentration, and interaction between atmosphere, ocean, and vegetation [*Ganopolski et al.*, 1998]. The northern winter season is slightly cooler (0.5–1°C) in a zone from
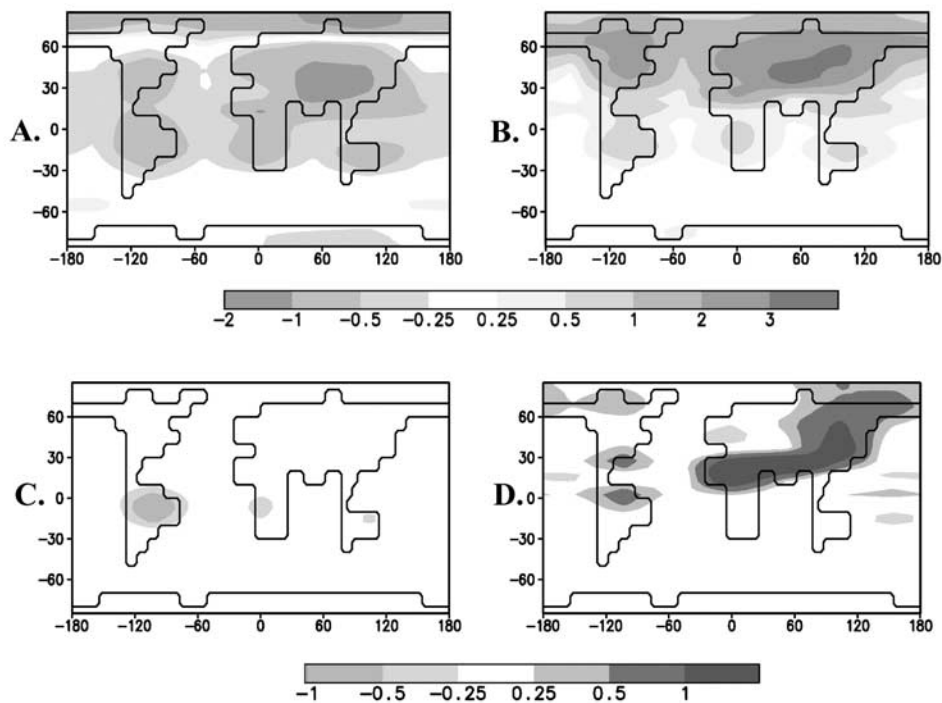
Figure 7. Climatic difference between AOVC-8K and AOVC-0K. (a) and (b) Change in near-surface air temperature (°C) for Northern Hemisphere winter (December–February) and summer (June–August), respectively. (c) and (d) Same as (a) and (b), respectively, but for change in precipitation (mm d^{-1}). See color version of this figure at back of this issue.

30°S to 60°N, especially over the continents (Figure 7a). This cooling was not observed in the mid-Holocene simulation with the previous CLIMBER-2 version [*Ganopolski et al.*, 1998], particularly because now we account for decreased atmospheric CO_2 concentration that corresponds to ca. 0.2°C global cooling. However, similar to our previous results, there is a winter warming up to 2°C over the Arctic ocean and continents north of 70°N, which is explained by the decreased sea ice area and sea ice-albedo feedback amplified via forest-temperature feedback. In this season (austral summer), there is a decline in precipitation over land in the tropics, which is especially significant (up to 1 mm d^{-1}) over southern America. This is mainly explained by a decrease in the land–ocean temperature gradient. As a result, lateral monsoon weakens and moisture convergence over continents decreases.

[26] During the northern summer, a warming of up to 3°C is pronounced over land in the Northern Hemisphere and tropical land in the Southern Hemisphere. A warming due to increased summer insolation is amplified by feedbacks between the components of the climate system (Figure 7b). Due to the large heat capacity of the ocean, seasonal changes in solar radiation result in much smaller temperature changes over the ocean than over the land. Summer precipitation increases significantly (by 1–1.5 mm d^{-1}) in the North Africa and in the Asian subtropical regions (Figure 7d), mainly as a result of intensified monsoon-type circulation which is amplified by vegetation-precipitation feedback [*Claussen and Gayler*, 1997; *Ganopolski et al.*, 1998]. The wetter conditions in the northern East Asia are explained by intensified monsoon-type circulation, increased forest cover, and subsequent increase in moisture convergence.

[27] In southern Europe, summer precipitation are lower by 0.5 mm d^{-1} due to several reasons. First, westerlies in the middle latitudes in the Northern Hemisphere are reduced in summer due to (1) a decrease in the equator-to-pole temperature difference and (2) development of a cyclone-type component of atmospheric circulation around North Africa in response to a lowering of the sea level pressure. Weakening of westerlies reduces eastward moisture flux in spite of intensified evaporation over Atlantic. Second, a development of the ascending branch of vertical velocity in low and middle troposphere over North Africa is compensated in the model via formation of correspondent descending branch over southern Europe, which suppress precipitation over the latter region. Third, an increase in the surface air temperature over the land is more pronounced than over the ocean. All factors contribute to a noticeable decrease in the relative humidity over southern Europe.

[28] Changes in the annual near surface air temperature are 0.1°C and 0.2°C for the globe and the Northern Hemisphere, respectively. Changes in the temperature over the Southern Hemisphere and global sea surface temperature (SST) are negligible. The hypothesis of decreased SSTs during the early Holocene discussed by *Indermühle et al.* [1999] is not supported by CLIMBER-2 simulation. The thermohaline circulation in the northern Atlantic is slightly weaker (by 0.2 Sv).

3.1.2. Changes in Vegetation Cover and Terrestrial Carbon Balance

[29] Changes in the vegetation structure (AOVC-8K minus AOVC-0K) are presented in Figure 8. Most remarkable changes in terms of vegetation cover are seen in the Afro-Asian northern subtropical regions, northeastern Asia and high northern latitudes.

[30] Changes in vegetation cover are the most noticeable in the Sahel/Sahara region (Figure 8a). The desert fraction inside the Sahara declines to 0.2, the rest of the area is covered by a mixture of C_3 (80%) and C_4 (20%) grasses. More abundant vegetation in the Sahara in the early Holocene is evident from different proxy data [*Hoelzmann et al.*, 1998; *Jolly et al.*, 1998; *Prentice et al.*, 2000]. The intensified monsoon-type circulation leads to an increase in tree fraction in the Sahel region, southern and eastern Asia (see Figure 8b). Due to a warmer summer the tree fraction increases by up to 0.3 in the northern subpolar region (averaged increase in the zone 60°–70°N is 0.2). This warming is partly explained by forest-temperature feedback in the region (presence of forest modifies the radiative balance during the snow season) [see *Otterman et al.*, 1984; *Foley et al.*, 1994; *TEMPO*, 1996; *Texier et al.*, 1997; *Levis et al.*, 1999]. At the same time, in southern Europe the tree fraction is lower by 0.1 due to an increase in the summer aridity. Similar changes reveal in subtropical regions in the Southern Hemisphere.

[31] Increased summer aridity and the subsequent decrease in tree fraction in southern and central Europe is explained by a decrease in relative air humidity during the summer season. Pollen reconstructions of vegetation cover reveal reverse changes in southern Europe, for example enhanced deciduous forest cover in the circum-Mediterranean region at the mid-Holocene [*Cheddadi et al.*, 1997; *Tarasov et al.*, 1998; *Prentice et al.*, 2000]. At the same time, at several sites in central and southeastern Europe where present-day "potential" vegetation is forest, a paleosol reconstruction method indicates early Holocene formation of black soil (Schwarzerde or Chernozem), a typical grassland soil [*Bork et al.*, 1998; *Alexandrovsky and Chichagova*, 1998]. Similar to the model results, the paleoreconstruction methods reveal that the amplitude of changes in forested area in the region was not considerable.

[32] Changes in NPP are shown in Figure 8c. NPP increases significantly in North Africa and in East Asia (up to 0.3 kgC m^{-2}) as a result of wetter climate. At the same time, NPP in southern Europe and in the southern subtropics slightly decreases. This decrease is caused by a decline in precipitation and a lower atmospheric CO_2 concentration. Globally integrated NPP is higher by 3.1 PgC yr^{-1}.

[33] Changes in vegetation cover and NPP transform into a complex picture of changes in total carbon storage (see Figure 8d). Global carbon storage increases by 90 Pg. The most significant increase in the total carbon storage (from 1 to 8 kgC m^{-2}) occurs in northern subtropical regions due to decreased aridity. In the Sahara region, soil carbon storage increases by 2.5 kgC m^{-2} while changes in biomass are much lower (0.4 kgC m^{-2}). In the Sahel, storage increases by 2 and 4 kgC m^{-2} for biomass and soil, respectively.
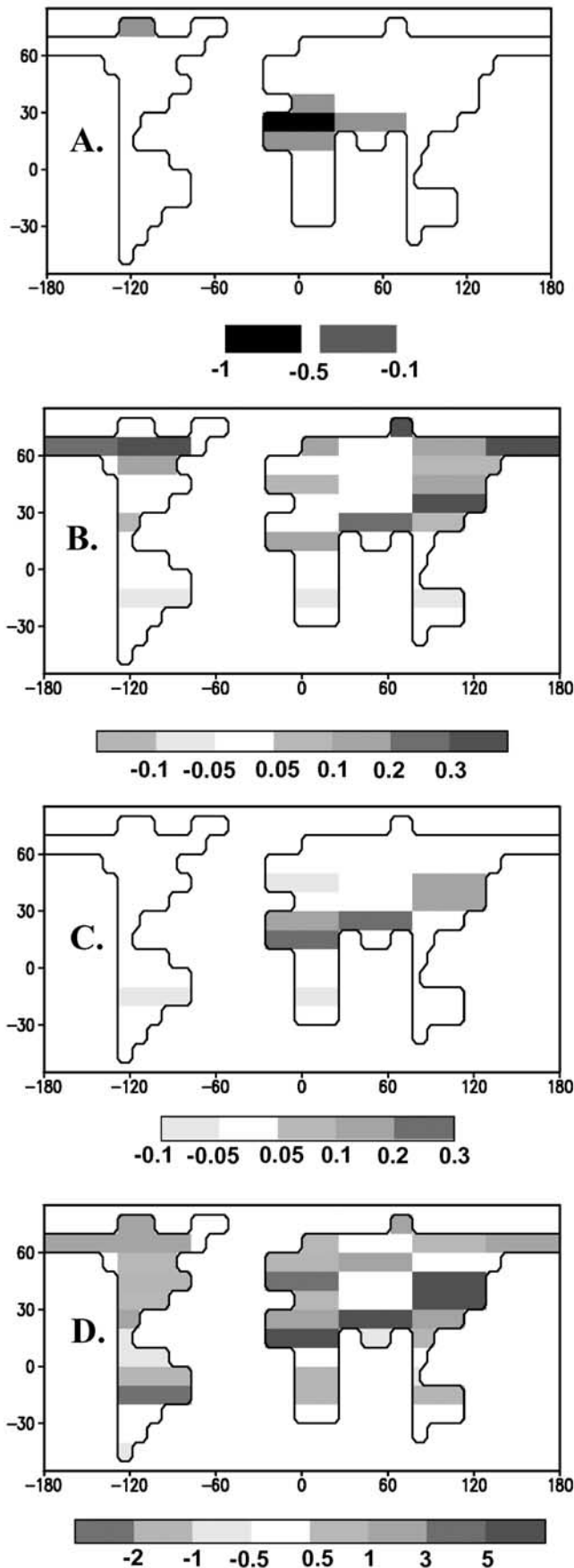
Similar increase is seen in South Asia. In southern Europe, the losses due to increased aridity are 1.3 and 1.4 kgC m^{-2} for biomass and soil, respectively. The southern tropical regions (0°–20°S) are a source of carbon as well, due to a decrease in NPP.

[34] In the northern high latitudes, the increase in carbon storage is not as pronounced as the increase in tree fraction. In terms of mean values over the zone 60°–70°N, the biomass increases by 1.3 kgC m^{-2} while the soil carbon decreases by 0.5 kgC m^{-2}. The latter is caused by a replacement of tundra with forest, as simulated soil carbon storage for trees is on average by 3 kgC m^{-2} lower than the soil carbon storage for grass.

[35] Two additional sensitivity experiments are performed to analyze the relative role of changes in climate and CO_2 in altering the terrestrial and oceanic carbon budget. Our approach is similar to the method by *Cramer et al.* [2001]. In the first simulation (AOVC-0K-co2), the carbon cycle is driven by a CO_2 concentration of 260 ppmv while the physical climate components simulate the preindustrial climate from AOVC-0K simulation (see Table 1). In the second simulation (AOVC-8K-clm), the terrestrial carbon responds to a preindustrial CO_2 concentration (280 ppmv) while the atmosphere/ocean components simulate AOVC-8K climate. The AOVC-0K-co2 simulation reveals effect of changes in atmospheric CO_2 concentration ("CO_2 only"), while the AOVC-8K-clm simulation demonstrates an effect of climatic changes ("climate only"). Changes in terrestrial carbon balance in the simulations are presented in Table 4. In the AOVC-0K-co2 simulation, lower atmospheric CO_2 lead to a decrease in NPP by 1.5 PgC yr^{-1} (see (A5)). Consequently, carbon storage in biomass and soil decreases, and total terrestrial carbon storage eventually reduces by 49 PgC (see Table 4). In contrast, the "climate only" simulation reveals an increase in NPP, biomass, and soil carbon, with total gain in 145 PgC. Therefore, changes in the atmospheric fields are more important for the terrestrial carbon budget than the changes in the atmospheric CO_2.

[36] We compare our results with other model assessments of the terrestrial carbon budget for the early to middle Holocene. Inverse modeling approach by *Indermühle et al.* [1999] (which is based on double deconvolution of Taylor Dome data) revealed a higher terrestrial carbon storage by 195 Pg at 8 kyr B.P. relative to preindustrial. In comparison with this estimation, changes within CLIMBER-2 (90 PgC) are smaller in amplitude while qualitatively in the same direction. Regarding experiments with prognostic models for the terrestrial biosphere, differences in the design of experiments are so significant that direct comparison can be misleading. Most simulations were done with "off-line" climate change scenarios, i.e., without accounting for biogeophysical feedbacks. For example, *Foley* [1994] found a 40 PgC increase in terrestrial carbon storage in an experiment with the DEMETER model using a mid-Holocene climate

Figure 8. (opposite) Difference in vegetation characteristics between AOVC-8K and AOVC-0K. (a) Desert fraction. (b) Tree fraction. (c) NPP (kgC m^{-2}). (d) Carbon storage (kgC m^{-2}). See color version of this figure at back of this issue.

Table 4. Changes in the Carbon Balance, Difference Between Sensitivity Simulations and AOVC-0K

Simulation	NPP (PgC yr^{-1})	Biomass (PgC)	Soil (PgC)	Total carbon (PgC)	DIC (PgC)
AOVC-8K-co2	−1.5	−17	−31	−48	−240
AOVC-8K-clm	5.4	63	79	142	−10
AOVC-8K	3.7	44	46	90	−250

simulated by the GENESIS model (atmospheric CO_2 was not changed). *Francois et al.* [1999] using the CARAIB model simulated a lower terrestrial carbon storage by 132 and 31 PgC at 6 kyr B.P. relative to preindustrial for the climate changes simulated by the ECHAM and LMD-LSCE models, respectively (atmospheric CO_2 concentration was changed from 280 to 260 ppmv). *Beerling* [2000] found a decrease in the terrestrial carbon storage of $265-370$ PgC in experiments using the SDGVM model for the climate changes simulated by the UGAMP model for the mid-Holocene. In the latter experiment, a significant part of the carbon loss was presumably a response to a decrease in the atmospheric CO_2 concentration from 350 ppmv to 280 ppmv.

[37] Changes in atmospheric $\delta^{13}C$, alteration in vegetation distribution and productivity, all lead to changes of $\delta^{13}C$ in the terrestrial carbon storage. Replacement of C_3 plants with C_4 plants and vice versa are especially noticeable in the Sahara/Sahel region. In the Sahel, ca. 20% of C_4 grasses are replaced by C_3 trees. In Sahara, C_4 grasses make up 25% of the vegetation cover. On a global scale, changes in distribution of C_3-C_4 plants lead to a slight decrease of terrestrial ^{13}C by 0.05‰. However, because of an increase in atmospheric $\delta^{13}C$ by 0.1‰ in the simulation, the overall effect is an increase in terrestrial ^{13}C by 0.05‰.

3.1.3.   Changes in Oceanic Biogeochemistry

[38] Alterations in the distribution of biogeochemical tracers in the ocean follow changes in physical fields (oceanic circulation, temperature) as well as changes in the atmospheric CO_2. In response to warmer SSTs in the North Atlantic, global oceanic NPP increases by 0.5 PgC yr^{-1} and new production increases by 0.1 PgC yr^{-1}. Simulated changes in the alkalinity and phosphate distributions are insignificant. In response to the prescribed increase in atmospheric $\delta^{13}C$ by 0.1‰ the average oceanic $\delta^{13}C$ increases by the same value. The total DIC storage in the ocean is 250 PgC lower than in (AOVC-0K) while changes in the DOC inventory are insignificant (increase of 2 PgC).

[39] The relative role of changes in climate and CO_2 for the ocean carbon cycle is explored in the sensitivity simulations AOVC-0K-co2 (CO_2 only) and AOVC-8K-clm (climate only). In the AOVC-0K-co2 simulation, DIC decreases by 240 Pg (see Table 4) due to a lower atmospheric CO_2 concentration. In the AOVC-8K-clm simulation, the oceanic DIC and DOC storages decrease by 10 Pg due to changes in SST and biogeochemical fields. Therefore, changes in the CO_2 boundary conditions are more important for the oceanic carbon budget than the changes in the SST and biogeochemical fields.

3.1.4.   Initial Conditions for the Transient Simulation

[40] Summarizing the global carbon balance, there is 200 Pg carbon less in (AOVC-8K) relative to (AOVC-0K) due to changes in the oceanic, terrestrial and atmospheric carbon storages of −250, 90, and −40 Pg, respectively (see Table 5). If the biogeochemical fields from the AOVC-8K simulation were taken as initial conditions for the transient simulation from 8 kyr B.P. to preindustrial, the initial deficit of 200 PgC would be transformed into too low carbon content of every compartment at the end of the simulation. With a sensitivity of the oceanic DIC storage to the atmospheric CO_2 of 240 Pg C per 20 ppmv (see Table 4, simulation AOVC-0K-co2), the final CO_2 concentration for the preindustrial would be about 270 ppmv instead of 280 ppmv (neglecting carbonate compensation).

[41] Another important point is that the carbonate ion concentration in the deep ocean is increased by 5 μmol kg^{-1} in the simulation AOVC-8K against the preindustrial simulation (see Table 1). This increase is explained by a decrease in the oceanic DIC storage while the alkalinity was kept constant. If the carbonate compensation were accounted for, the ocean alkalinity and DIC storage would be lower than in the AOVC-8K simulation. This would lead to even larger carbon imbalance in comparison with the AOVC-0K simulation. However, proxy for the carbonate ion concentration [*Broecker et al.*, 1999] suggest that its value was higher during the early Holocene. Presumably, this increase is explained by CO_2 release from the ocean during glacial–interglacial transition and a deepening of saturation horizon for calcite. The oceanic carbonate system had reacted by excessive accumulation of $CaCO_3$ sediments and restoring of the carbonate ion concentration in the deep ocean. Because of the long timescale of this process (ca. 5000 years), at the early Holocene the oceanic carbonate system was not in equilibrium and the carbonate compensation led to the excessive carbonate accumulation during the Holocene [*Milliman*, 1993]. Another mechanism for explaining alkalinity changes during the Holocene could be a regrowth of coral reefs [*Milliman*, 1993].

[42] While modeling of ocean sediments and regrowth of coral reefs is not implemented into the current version of CLIMBER-2, we imitate these processes by removing a fraction of the biogenic $CaCO_3$ flux above the lysocline (assumed to be at 3.5 km depth). This process immediately removes dissolved carbon in proportion of one mole of DIC per two moles of ALK. On a long timescale, an additional DIC is outgassing to the atmosphere due to decreased alkalinity (this process is simulated explicitly). Consequently, ALK and DIC must be increased for simulation of the initial conditions.

[43] It is also necessary to equalize the total carbon storage for the initial and final time slices. Accounting for the DIC storage sensitivity to the alkalinity and a ratio

Table 5. Changes in Global Carbon Balance, Difference Between AOVC-8K-H and AOVC-0K

Compartment	Carbon content (Pg)
Atmosphere	−40
Ocean DIC and DOC	220
Ocean $CaCO_3$ sediment	−270
Land biosphere	90
Total	0

between the alkalinity and $CaCO_3$, we found that with a mean oceanic alkalinity increased by 33 μeq kg^{-1} (ca. 1.3%) the total oceanic carbon storage within the model is higher by 220 Pg than in (AOVC-0K). Changes in the global carbon cycle components in this simulation AOVC-8K-H (H is for high alkalinity) are shown in Table 5. The total amount of carbon in (AOVC-8K-H) is the same as in (AOVC-0K) including excessive $CaCO_3$ sediments, therefore it can be used as initial conditions for the transient simulation through the Holocene. Sedimentation of $CaCO_3$ (270 PgC) is necessary to decrease the ocean alkalinity to the preindustrial value. The difference in the carbonate ion concentration between (AOVC-8K-H) and (AOVC-0K) for the deep tropical ocean is ca. 8 μmol kg^{-1} (see Table 1). The latter is similar to an estimate of 11 ± 2 μmol kg^{-1} obtained from size distribution of the early Holocene oceanic carbonate sediments by *Broecker et al.* [1999].

3.2. Transient Simulations From 8 kyr B.P. to Preindustrial

[44] In the transient simulation AOVC-T all the components of the climate system (atmosphere, ocean, land vegetation, oceanic and terrestrial carbon cycles) evolve interactively under the slow changes in the orbital forcing. A scenario of oceanic $CaCO_3$ sedimentation is another external forcing in the simulation. We assume that a fraction of the $CaCO_3$ flux does not dissolve above the lysocline:

$$f_{sed} = p_{sed} \exp\left(-\frac{t}{\tau_{sed}}\right), \qquad (1)$$

where τ_{sed} is a timescale of carbonate compensation (5000 years) and p_{sed} is taken as 0.18 in order to accumulate 270 PgC during the whole simulation. The initial conditions are taken from (AOVC-8K-H).

3.2.1. Climate, Carbon, and Vegetation Dynamics on a Global Scale

[45] Results of the transient simulation relative to (AOVC-0K) in terms of zonal average over the land for several model characteristics (insolation, summer warmth, tree fraction and total carbon) are presented in Figure 9. The changes in summer insolation due to alteration in orbital parameters is especially noticeable at the northern temperate and high latitudes (up to 30 W m^{-2} at 8 kyr B.P., see Figure 9a), where insolation declined smoothly from early Holocene to present [*Berger*, 1996]. The changes in insolation during the last 2000 years are insignificant. Summer warmth expressed in terms of degree days above 0 (GDD0) steady declines in middle and high northern latitudes. In the early to middle Holocene, northern subtropical regions are slightly cooler than at the end of the simulation particularly because of expanded vegetation cover and larger evapotranspiration. During the last 2000 years, changes in GDD0 are negligible (see Figure 9b).

[46] On a global scale, annual mean surface air temperature is nearly steady between 8 and 6 kyr B.P.; it declines by 0.1°C during the next 2000 years and remains steady after 4 kyr B.P. (see Figure 10a). In the Northern Hemisphere, the temperature follows the trend of global temperature between 8 and 4 kyr B.P., then has minimum around 3 kyr B.P. and increases again to the preindustrial value
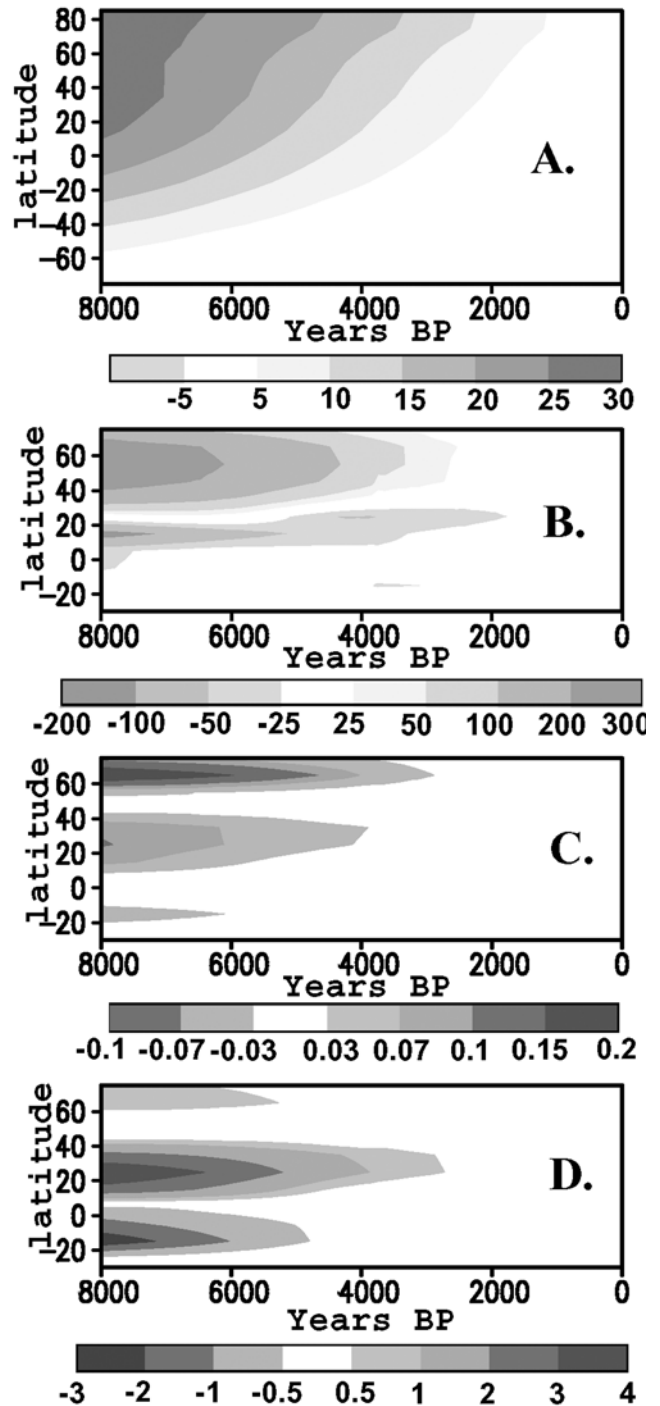

Figure 9. Changes in climate, vegetation, and carbon characteristics, difference between AOVC-T) and (AOVC-0K. (a) Summer irradiation (W m^{-2}), external forcing. (b) Growing degree days (GDD0). (c) Tree fraction. (d) Carbon storage (kgC m^{-2}). See color version of this figure at back of this issue.

around 500 years BP (Figure 10b). Southern Hemisphere exhibits a different kind of dynamics. Temperature reaches a maximum around 6 kyr B.P., then declines and stays almost constant for last 3000 years (Figure 10c). The response of
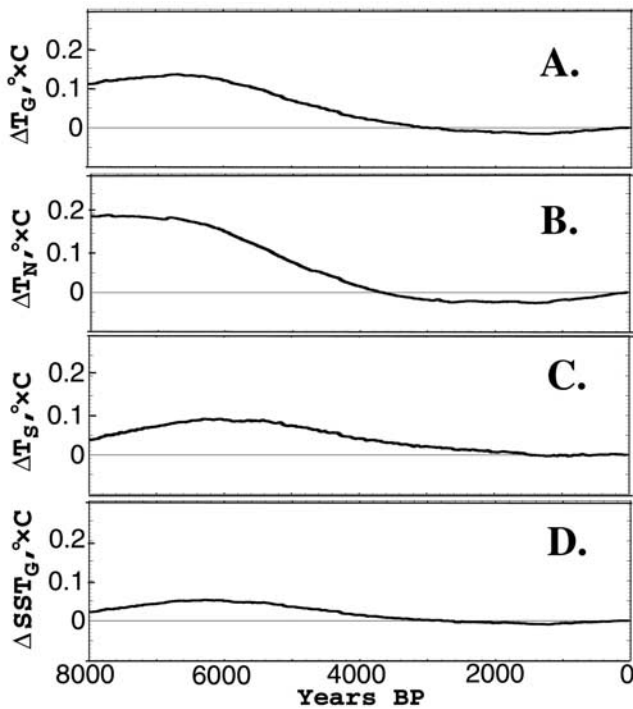
Figure 10. Changes in mean annual surface temperature (°C), difference between AOVC-T and AOVC-0K. (a) Globe. (b) Northern Hemisphere. (c) Southern Hemisphere. (d) Global SST.

Figure 11. Global vegetation cover (10^6 km^2) (AOVC-T). (a) Trees. (b) Grasses. (c) Desert.

the global mean SST is similar to the response of the Southern Hemisphere temperature but with smaller amplitude (0.05°C, see Figure 10d).

[47] The changes in zonally averaged tree fraction are most significant in the northern high latitudes. Decline in the tree fraction follows the trend of GDD0 in this region (Figure 9c). Similarly, in the northern subtropics changes in tree fraction follow changes in precipitation (not shown). At the same time, changes in the southern subtropics are opposite because the region is drier in the early Holocene.

[48] On a global scale, the area covered by trees declines during 8–4 kyr B.P. from 64 to 57 million km^2 and remains nearly constant during last 2000 years (Figure 11a). Desert area grows significantly from 15 to 23 million km^2 (excluding Antarctica) with most of the changes occurring during 6–4 kyr B.P. (Figure 11c). A decrease in grass area (from 58 to 56 million km^2) is less significant than the reduction in tree area, because a decrease of grass area in Sahara is compensated by the replacement of trees by grass in Sahel and increase in tundra area at the northern high latitudes. Most of the changes in grass area occur during 6–4 kyr B.P. following aridization of North African climate (Figure 11b).

[49] In terms of terrestrial carbon storage, changes are more significant in the subtropical regions than in the northern high latitudes (Figure 9d). Decline in carbon storage in the Northern Hemisphere is followed by a simultaneous buildup of carbon storage in the Southern Hemisphere. During the last 3000 years of the simulation the storages are relatively steady. This is explained by simultaneous changes in climate and atmospheric CO$_2$.
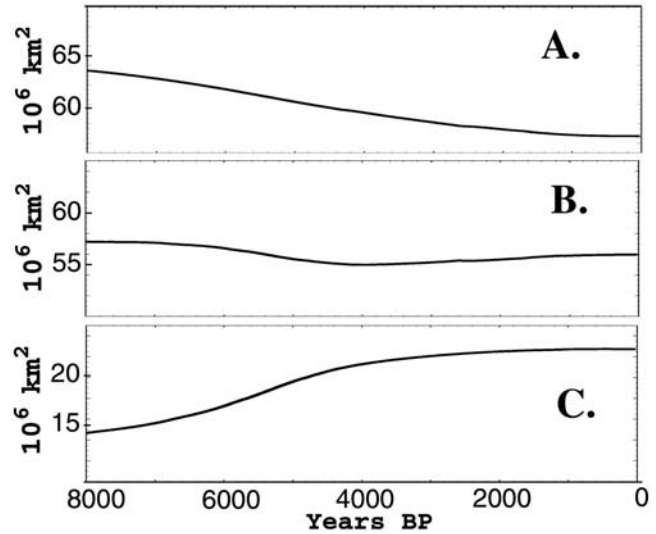
On a global scale, most significant changes in the terrestrial carbon storage occur during 7–4 kyr B.P., while the last 2000 years the storages are nearly constant (Figure 12).

[50] Changes in C_{atm} (Figure 13a) are explained by changes in the terrestrial and the oceanic carbon pools (Figure 12a). During 8–7 kyr B.P., the terrestrial carbon pool declines due to changes in vegetation cover and C_{atm} increases by 4 ppmv during that period, well in line with Taylor Dome data. During 7–4 kyr B.P. the decline in land carbon storage of ca. 80 Pg leads to an increase in C_{atm} by additional 10 ppmv (Figure 13a) and simultaneous decline in atmospheric δ^{13}C by 0.05‰ (Figure 13b). During the next 4000 years, the oceanic total carbon storage (including
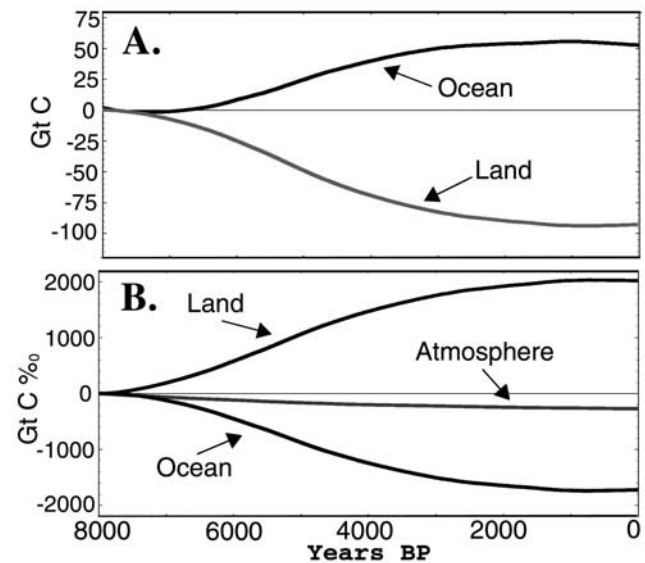

Figure 12. Changes in oceanic (including CaCO$_3$ sediments) and terrestrial carbon storages (AOVC-T). (a) Total carbon (PgC). (b) ^{13}C (PgC ‰).
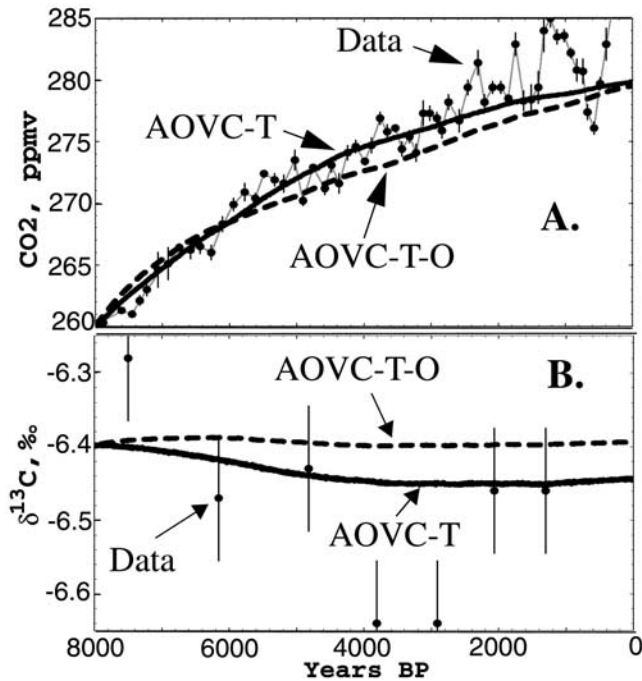
Figure 13. Comparison of Taylor Dome data [*Indermühle et al.*, 1999] and transient simulations for atmospheric CO_2 and $\delta^{13}C$. (a) Dynamics of atmospheric CO_2 concentration (ppmv). Solid line for AOVC-T simulation (both terrestrial and oceanic carbon sources), dashed line for AOVC-T-0 simulation (oceanic carbon source only), and dots with $1 - \sigma$ error bars and thin line for the ice core data. (b) Same as (a), but for $\delta^{13}C$ (‰).

CaCO$_3$ sediments) slowly grows due to absorption of the released terrestrial carbon. Atmospheric $\delta^{13}C$ in this period remains steady as $\delta^{13}C$ emitted by land is absorbed by the ocean (see Figure 12b).

[51] During the last 1000 years of simulation C_{atm} approaches 280 ppmv. At the end of the simulation the carbon storages are nearly steady: terrestrial biosphere carbon uptake is 0.02 PgC yr^{-1}, while release from the ocean is 0.025 PgC yr^{-1}. Let us note that we do not account for anthropogenic, solar and volcanic forcings which influenced the climate considerably during the last 1000 years [*Brovkin et al.*, 1999; *Crowley*, 2000].

3.2.2. Regional Vegetation Dynamics

[52] In the two land regions simulated to have the most pronounced vegetation changes, i.e., northern Africa and the northern high latitudes, we compare the model results with available continuous records of proxy data.

[53] In the Sahara region, vegetation fraction within the model declined from ca. 0.8 at 8 kyr B.P. to almost 0 at 3 kyr B.P. The decrease in vegetation cover is especially rapid during 6–4.5 kyr B.P. This desertification is a result of a more arid climate amplified by vegetation–atmosphere interaction. Comprehensive analysis of the model performance in the Sahara region (e.g., role of ocean interaction in the system dynamics) is presented in detail by *Claussen et al.* [1999b]. Model results compare favorably with the recently analyzed record of aeolian sedimentation at the

coast of West Africa which reveals a rapid termination of the African Humid period at the time around ca. 5500 years BP [*deMenocal et al.*, 2000].

[54] In the northern high latitudes, pollen data and macrofossils are the main proxy data available for comparison with the model [*Velichko et al.*, 1997; *MacDonald et al.*, 2000]. Here, we present two continuous Holocene pollen records in lake sediments analyzed recently at the Alfred-Wegener-Institut für Polar- und Meeresforschung in Potsdam. Selected pollen taxa are shown in Figure 14. The Lama Lake (70°N, 90°E) is situated in the northern taiga near the northern limit of present-day tree line and the Levinson-Lessing Lake (74°N, 98°E) is located in the southern tundra near the boundary with typical Arctic tundra. At the first site, *Picea obovata* (siberian spruce) pollen is abundant in the pollen records for the period from 8 kyr B.P. to ca. 3 kyr B.P. and its percentage declines after 3 kyr B.P., while *Larix* (larch) pollen percentage shows some increase after 4 kyr B.P. (Figure 14a). The total tree pollen fraction declines after 4 kyr B.P. For the last 2000 years, there is a significant variability in total tree pollen fraction while its mean level is rather low in comparison with the early Holocene.

[55] At the second site, *Alnus fruticosa* (shrub alder), the main arboreal representative in the pollen records, shows significant decline in the pollen percentage during 8–4 kyr B.P. (Figure 14b). Similar changes are seen for *Betula* sect.
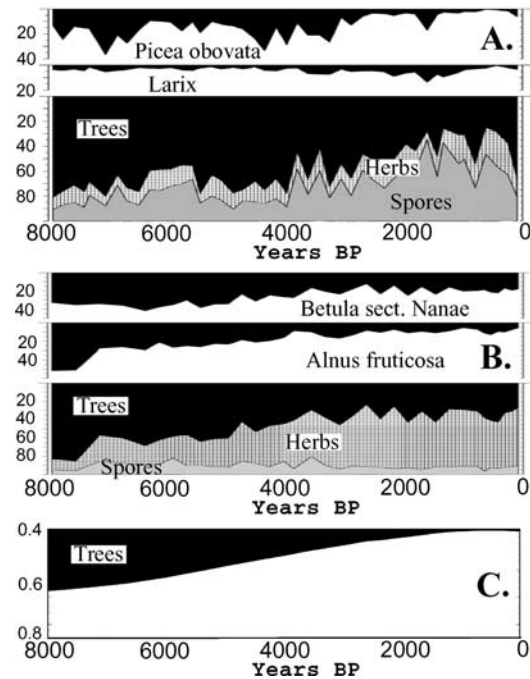

Figure 14. Comparison of pollen records and CLIMBER-2 results for boreal region. (a) Pollen diagram for the Lama Lake (70°N, 90°E). Black shaded area is for percentages of pollen content of selected tree species and total pollen percentage of trees against herbs pollen and spores percentages. (b) The same as (a), but for the Levinson-Lessing Lake (74°N, 98°E). (c) Simulated tree fraction (AOVC-T), zone 60–70°N.

Nanae (dwarf birch). During the last 3000 years, the tree and shrub pollen percentages show little changes, reflecting a treeless environment around the site.

[56] Because of the coarse model's spatial resolution and high spatial variability of vegetation cover in the area, data and model can be compared only in qualitative terms. Changes in the simulated averaged tree fraction in the zone $60°-70°N$ are shown in Figure 14. Qualitatively, a decline in tree cover evident from the pollen records is in line with the model results. Simulated tree fraction exhibits gradual decline from 0.6 to 0.4, with main changes occur during $8-3$ years BP (Figure 14c). The main driving force for this decline is the slow cooling over the area which is most pronounced in summer. Climatic reconstruction based on the pollen data from the Taymyr peninsula [*Andreev and Klimanov*, 2000] reveals gradual summer cooling from the early Holocene to present-day; changes in winter temperature are not so pronounced in the reconstruction. Besides, the reconstruction shows high interannual variability in climate. Let us note that simulated climate variability is less than the observed variability as the model was designed to simulate the mean climate trend.

3.2.3. Transient Simulation With the "Ocean Only" Carbon Source Scenario

[57] Since submitting this paper, an article by *Broecker et al.* [2001] about causes of the rise of the atmospheric CO_2 content during the last 8000 years has been published in the G^3, an electronic journal of the AGU. *Broecker et al.* [2001] supported their previous hypothesis that the rise of the atmospheric CO_2 was caused by the oceanic carbonate compensation with additional proxies. They also presented a scenario of changes in the atmospheric CO_2 and $\delta^{13}C$ in accordance with their hypothesis. Although release of 90 PgC of terrestrial carbon in the AOVC-T simulation is a result consistent with the simulated climatic changes, it is interesting to compare the scenario by *Broecker et al.* [2001] with CLIMBER-2 results for the "ocean only" carbon source scenario. We performed additional transient simulation (AOVC-T-O) in which an influence of terrestrial biosphere on the carbon balance was neglected for both, atmospheric CO_2 and $\delta^{13}C$. Because in this case the land source of 90 PgC was not accounted for, the initial conditions for alkalinity were changed in order to equalize initial and final values of the total carbon storage. Applying procedure similar to the AOVC-8K-H simulation, we found that with the mean alkalinity of 2421 μeq kg^{-1} the total carbon storage is equal to the total amount of carbon in the AOVC-0 simulation plus 390 PgC of carbonate sediments which are necessary for the alkalinity changes. The sedimentation forcing during transient simulation was prescribed by (1) where p_{sed} was taken as 0.25 in order to accumulate 390 PgC during the whole simulation. Another equilibrium simulation, (AOVC-8K-O), was done to provide the transient simulation with the initial conditions (see Table 1). The increase of carbonate ion concentration in the deep ocean in this simulation is 9.5 μmol kg^{-1}. This value is nearly identical to an estimate of 10 μmol kg^{-1} presented by *Broecker et al.* [2001].

[58] Results of the AOVC-T-O simulation are shown in Figure 13. Simulated atmospheric CO_2 concentration is generally in line with the Taylor Dome data, although after 5000 years BP the simulated trend is at the bottom of the data scatter. Similar to the scenario by *Broecker et al.* [2001], atmospheric $\delta^{13}C$ is not significantly affected (Figure 13b) because (1) $\delta^{13}C$ of carbonate is similar to an average oceanic $\delta^{13}C$ and (2) fractionation of $\delta^{13}C$ due to sea surface–atmosphere CO_2 exchange is not considerably changed.

[59] Comparing results of AOVC-T and AOVC-T-O simulations, it is difficult to decide which of them is more consistent with the available proxy data. Regarding initial carbonate ion concentration, the AOVC-T-O simulation is more closed to the proxy while the difference between the simulations (1.5 μmol kg^{-1}) is smaller than the proxy precision (2 μmol kg^{-1}) [*Broecker et al.*, 1999]. Trend of the atmospheric CO_2 concentration is nearly identical in both simulations until 6 kyr B.P., while later the AOVC-T simulation is more close to the observations (see Figure 13a). The difference between simulations has maximum around 4 kyr B.P. when most of the terrestrial carbon storage is released within the model (see Figure 12). However, the amplitude of this difference (3 ppmv) is comparable with the scatter of the data. Atmospheric $\delta^{13}C$ is declining in the AOVC-T simulation, similar to the proxy data, but the amplitude of changes is much smaller than in the data (Figure 13b). The AOVC-T-O simulation does not reveal changes in $\delta^{13}C$, contrary to the proxy. However, the argument made by *Broecker et al.* [2001] about technical difficulties with measurement of $\delta^{13}C$ is in favor of possibility that there was no measurable trend in $\delta^{13}C$ of atmospheric CO2 during the last 8000 years. Let us note that the difference between AOVC-T and AOVC-T-O simulations is less than the uncertainty in measuring $\delta^{13}C$.

[60] We conclude that the difference between two transient simulations is comparable with an uncertainty in the proxy data. Based on the available proxies for the atmospheric CO_2, $\delta^{13}C$, and oceanic carbonate ion concentration, it is not possible to answer on the question whether the atmospheric CO_2 rise during the last 8000 years was caused by the ocean response only or decay of terrestrial carbon has contributed to this rise as well. More proxies are needed to address this question.

4. Discussion and Conclusions

[61] Our transient experiment is to our knowledge the first simulation of the global carbon cycle within the framework of a climate system model on a millennium timescale. The simulation is different from experiments on a century timescale [*Cox et al.*, 2000; *Dufresne et al.*, 2001] because slow long-term processes in the global biogeochemistry (e.g., carbonate sedimentation) are important on a millennium timescale. We set up the initial conditions for the transient experiment in two steps. First, we conducted two equilibrium experiments for initial and final time slices and estimated changes in the oceanic and terrestrial carbon storages while the atmospheric CO_2 concentration was prescribed to the observed values. Then we used an assumption about long-term processes to equalize the total carbon storage for both time slices. Thus, initial conditions

guarantee us a proper amplitude of changes in atmospheric CO_2 concentration while changes in $\delta^{13}C$ are not controlled by the experiment design.

[62] Our major conclusion is that changes in the orbital forcing could explain most of the observed long-term dynamics of climate–vegetation system during the Holocene. The most significant changes in vegetation cover during Holocene occurred in monsoon regions in the northern subtropics, above all in the North Africa. Model results compare favorably with the proxy data which reveals very rapid desertification of the Sahara/Sahel region during 6–5 kyr B.P. [*deMenocal et al.*, 2000]. This abruptness can be explained by the atmosphere–vegetation interaction which amplifies the decrease in precipitation due to changes in the orbital forcing [*Claussen et al.*, 1999b]. In eastern Asia, a simulated increase in tree fraction in middle Holocene due to intensified monsoon circulation is in line with proxy data [*Prentice et al.*, 2000].

[63] The northern circumpolar region is another region with a remarkable change in vegetation cover during the Holocene. Continuous pollen records for Taymyr peninsula reveal a decrease in tree pollen during 8–3 kyr B.P. while rather stable vegetation cover during the last 3000 years. Qualitatively, model results are in line with data. Decline in tree fraction within the model could be interpreted as either a southward retreat of the tree line or a reduction in forest density, or a combination of the two. In North America, the model shows a significant decrease in tree fraction during the Holocene due to summer cooling of 1–2°C. However, proxy data reveal little shift in tree line position in the Arctic [*Prentice et al.*, 2000]. One possible explanation for this difference is the impact of a relatively late decay of the Laurentide ice sheet on regional climate and soil formation, which we neglect in our simulation.

[64] The model simulations reveal that terrestrial carbon storage at 8 kyr B.P. was 90 PgC higher than preindustrial storage. Most of these changes are explained by changes in vegetation cover in the northern subtropics where more humid climate was favorable for plant productivity. Changes in vegetation cover in the circumpolar region, although significant, were not subsequently followed by a significant increase in carbon storage because of relatively low productivity of plants in the arctic environment. In some other regions, especially in the Southern Hemisphere, terrestrial carbon storage was reduced due to the low atmospheric CO_2 concentration during the early Holocene.

[65] With a preindustrial value for the mean ocean alkalinity the model can not reproduce the amplitude of CO_2 changes in the Holocene recorded in the ice cores. Accounting for excessive $CaCO_3$ sedimentation in the ocean is necessary to explain the atmospheric CO_2 trend inferred from the ice cores. A higher concentration of carbonate ion in the deep ocean during the early Holocene is in accordance with sediment data [*Broecker et al.*, 1999]. Presumably, carbonate sedimentation process in the ocean during the Holocene led to a decrease in the carbonate ion concentration. As a consequence of declining alkalinity, the ability of the ocean to absorb carbon emitted by the terrestrial biosphere was reduced. Hence, in accordance to our model results, the ocean was a source of carbon during the late Holocene.

[66] In the transient simulation AOVC-T, atmospheric $\delta^{13}C$ decreases by 0.05‰ during the first half of the simulation in response to a decline in the terrestrial carbon storage. While this decrease is qualitatively in line with Taylor Dome data, the amplitude of changes in the model is much smaller than in the data (ca. 0.35‰). Possible explanations include (1) uncertainties in the measurements of ^{13}C (ca. 0.08‰), (2) long-term variability in oceanic or atmospheric circulation, which was not considered in our experiments, and (3) the biogeochemical processes neglected in the model, for example, methane emissions, which could considerably influence the atmospheric $\delta^{13}C$. Accounting for methane production as well as accumulation and decay of carbon in wetlands should improve carbon balance estimates in future model simulations.

[67] "Ocean only" carbon source scenario is addressed in the transient simulation AOVC-T-O. Simulation results are in line with a scenario of changes in the atmospheric CO_2 and $\delta^{13}C$ recently published by *Broecker et al.* [2001]. The difference between two transient simulations, AOVC-T and AOVC-T-O, is comparable with an uncertainty in the proxy data. Based on the available proxies for the atmospheric CO_2, $\delta^{13}C$, and oceanic carbonate ion concentration, it is not possible to conclude whether the atmospheric CO_2 rise during the last 8000 years was caused by the ocean response only or decay of terrestrial carbon has contributed to this rise as well. More proxies are needed to address this question.

Appendix A: Equations for Terrestrial Carbon Cycle

$$\Phi = \{t, g\}, \qquad \frac{dC_\Phi^1}{dt} = k_\Phi^1 \Pi \alpha_\Phi^* R^* - \frac{C_\Phi^1}{\tau_\Phi^1}, \qquad \text{(A1)}$$

$$\frac{dC_\Phi^2}{dt} = \left(1 - k_\Phi^1\right)\Pi \alpha_\Phi^* R^* - \frac{C_\Phi^2}{\tau_\Phi^2}, \qquad \text{(A2)}$$

$$\frac{dC_\Phi^3}{dt} = k_\Phi^2 \frac{C_\Phi^1}{\tau_\Phi^1} + k_\Phi^3 \frac{C_\Phi^2}{\tau_\Phi^2} - \frac{C_\Phi^3}{\tau_\Phi^3}, \qquad \text{(A3)}$$

$$\frac{dC_\Phi^4}{dt} = k_\Phi^4 \frac{C_\Phi^2}{\tau_\Phi^2} + k_\Phi^5 \frac{C_\Phi^3}{\tau_\Phi^3} - \frac{C_\Phi^4}{\tau_\Phi^4}, \qquad \text{(A4)}$$

$$\Pi(T_a, P_r, C_{atm}) = \Pi_{max} \min\left\{ \frac{1}{1 + e^{(\nu_1 - \nu_2 T_a)}} 1 - e^{\nu_3 P_r} \right\}$$

$$\cdot \left(1 + \beta \log \frac{C_{atm}}{C_{atm}^0}\right), \qquad \text{(A5)}$$

$$k_\Phi^1(\Pi) = n_\Phi^1 + \frac{n_\Phi^2}{1 + n_\Phi^3 \Pi}, \qquad \text{(A6)}$$

$$\tau_\Phi^i = \begin{cases} m_\Phi^{i,1} + \frac{m_\Phi^{i,2}}{1 + m_\Phi^{i,3}\Pi} & i = \{1, 2\}, \\ m_\Phi^{i,4} e^{-m_\Phi^{i,5} T_a} & i = \{3, 4\}, \end{cases} \qquad \text{(A7)}$$

$$\alpha_\Phi^* = R^* = 1 \text{ for } *C = {}^{12}C; \alpha_t^* = \alpha_3^{13},$$

$$\alpha_g^* = \alpha_3^{13}g_3 + \alpha_4^{13}(1 - g_3), R^* = \frac{{}^{13}C_a}{C_a} \text{ for } *C = {}^{13}C,$$

$$\frac{df}{dt} = \frac{1}{\tau_t^2}\left(\hat{f} - f\right), \tag{A8}$$

$$\frac{dv}{dt} = \frac{1}{\tau_v}(\hat{v} - v), \tag{A9}$$

$$\tau_v = \begin{cases} \tau_g^2 & v_{min} \leq v \leq 1, \\ \tau_t^2 & v < v_{min}, \end{cases} \tag{A10}$$

$$g = v - f, \hat{f}(G_0, P_r) = f_{max}\left(1 - e^{-c(G_0 - G_{min})}\right)$$
$$\cdot \frac{(P_r)^a}{(P_r)^a + a_{for}(G_0 - G_{min})^2 e^{b(G_0 - G_{min})}}, \tag{A11}$$

$$\hat{v}(G_0, P_r) = \begin{cases} 0 & P_r \leq P_r^{min}, \\ \min[1, \hat{V}] & P_r > P_r^{min}, \end{cases} \tag{A12}$$

$$\hat{V} = 1 - \frac{1}{1 + a_{des}\left(P_r - P_r^{min}\right)^2 e^{b(G_0 - G_{min})}}, \tag{A13}$$

$$P_r^{min} = P_r^0 e^{b_2(G_0 - G_{min})}. \tag{A14}$$

Appendix B: Equations for Oceanic Carbon Cycle (Except Sea Surface–Air Exchange)

$$\frac{\partial \Gamma}{\partial t} = A_d(\Gamma) + J_{org}(\Gamma) + J_{car}(\Gamma), \tag{B1}$$

$$\Gamma = \left\{C_{dic}, C_{doc}^i, {}^{13}C_{dic}, {}^{13}C_{doc}^i, {}^{14}C_{dic}, P, O_2, ALK\right\},$$
$$i = \{f, s\}, \frac{dC_p}{dt} = \Pi - G - (d_p + \gamma_p)C_p', \tag{B2}$$

$$\frac{dC_z}{dt} = \epsilon_{her}\zeta G - (d_z + \gamma_z)C_z', \tag{B3}$$

$$\Pi = r(T, L)\frac{P}{P + P^0}C_p, \tag{B4}$$

$$G = g_T(T)\frac{C_p'}{C_p + C_p^0}C_z, \tag{B5}$$

$$E(z) = (1 - \epsilon_{her})G + d_pC_p' + (1 - \epsilon_{can})d_zC_z', \tag{B6}$$

$$J_{org}(C_{dic}) = F_{dic} + D^f + D^s, \tag{B7}$$

$$J_{org}(C_{doc}^i) = F_{doc}^i - D^i, \tag{B8}$$

$$J_{org}(P) = \frac{F_{dic}}{\eta_{dic}(z)} + \frac{D^f + D^s}{\eta_{doc}}, \tag{B9}$$

$$J_{org}(O_2) = -F_{dic}\frac{\eta_{O_2}(z)}{\eta_{dic}(z)} - (D^f + D^s)\frac{\eta_{O_2}(z_{eup})}{\eta_{doc}}, \tag{B10}$$

$$J_{org}(ALK) = -F_{dic}\frac{\eta_N}{\eta_{dic}(z)}, \tag{B11}$$

$$J_{car}(ALK) = 2F_{car}, \tag{B12}$$

$$D^i = r_{doc}^i C_{doc}^i, \tag{B13}$$

$$C_p' = C_p - C_p^{min}, \tag{B14}$$

$$C_z' = C_z - C_p^{min}, \tag{B15}$$

functions $r(T, L)$ and $g_T(T)$ are from the work of *Six and Maier-Reimer* [1996, equations (1)–(4)], sources in euphotic layer:

$$F_{dic} = \left(-\Pi + \epsilon_{her}(1 - \zeta)G + \epsilon_{can}d_zC_z'\right)\alpha_{org}^*R^*, \tag{B16}$$

$$F_{doc}^i = l_f^i\left(\gamma_pC_p' + \gamma_zC_z'\right)\alpha_{org}^*R^*, \tag{B17}$$

$$F_{car} = -\kappa(z)R_rE(z)R^*, \tag{B18}$$

sources in aphotic layer:

$$F_{dic} = \frac{\partial\theta}{\partial z}\alpha_{org}^*R^*\int_0^{z_{eup}} E(z)dz, \tag{B19}$$

$$F_{car} = \frac{\partial\kappa}{\partial z}R_rR^*\int_0^{z_{eup}} E(z)dz, \tag{B20}$$

$$\theta(z) = \left(\frac{z}{z_{eup}}\right)^{a_\theta} \tag{B21}$$

$$\kappa(z) = e^{\left(-\frac{z - z_{eup}}{d_\kappa}\right)} \tag{B22}$$

$$F_{doc}^i = 0, \tag{B23}$$

$$J_{org}(O_2) = -F_{dic}\frac{\eta_{O_2}(z)}{\eta_{dic}(z)} - (D^f + D^s)\frac{\eta_{O_2}(z_{eup})}{\eta_{doc}}, \tag{B24}$$

$$J_r\left({}^{14}C_{dic}\right) = -\lambda^{14}C_{dic}, \tag{B25}$$

$$\alpha_{org}^* = R^* = 1 \text{ if } \Gamma = \left\{C_{dic}, C_{doc}^i\right\}, \alpha_{org}^* = \alpha_{org}^{13},$$
$$R^* = \frac{{}^{13}C_{dic}}{C_{dic}} \text{ if } \Gamma = \left\{{}^{13}C_{dic}, {}^{13}C_{doc}^i\right\}.$$

References

Adams, J. M., H. Faure, L. Faure-Denard, and J. M. McGlade, Increases in terrestrial carbon storage from the Last Glacial Maximum to the present, *Nature*, *348*, 711–714, 1990.

Alexandrovsky, A. L., and O. A. Chichagova, Radiocarbon age of Holocene paleosols of the east European forest–steppe zone, *Catena*, *34*, 197–207, 1998.

Andreev, A. A., and V. A. Klimanov, Quantitative Holocene climatic reconstruction from Arctic Russia, *J. Paleolimnol.*, *24*, 81–91, 2000.

Archer, D., A. Winguth, D. Lea, and N. Mahowald, What caused the glacial/interglacial atmospheric pCO$_2$ cycles?, *Rev. Geophys.*, *38*, 159–189, 2000.

Bacastow, R., and E. Maier-Reimer, Ocean-circulation model of the carbon cycle, *Clim. Dyn.*, *4*, 95–125, 1990.

Barnola, J. M., D. Raynaud, C. Lorius, and Y. S. Korotkevich, "Vostok" ice core atmospheric CO$_2$ concentration records, in *Trends '93 Database*, CDIAC, ORNL, Oak Ridge, Tenn., 1993.

Bazilevich, N. I., *Biological Productivity of Ecosystems of Northern Eurasia*, 293 pp., Nauka, Moscow, in Russian, 1993.

Beerling, D. J., The role of the terrestrial biosphere in Holocene carbon cycle dynamics, *Glob. Ecol. Biogeogr.*, *9*, 421–429, 2000.

Berger, A., Orbital variations, in *Encyclopedia of Climate and Weather*, edited by S. Schneider, pp. 557–564, Oxford Univ. Press, New York, 1996.

Blunier, T., and E. J. Brook, Timing of millennium-scale climate change in Antarctica and Greenland during the last glacial period, *Science*, *291*, 109–112, 2001.

Bork, H.-R., C. Dalchow, B. Faust, H.-P. Piorr, and Th. Schatz, *Landschaftsentwicklung in Mitteleuropa*, 328 pp., Klett-Perthes, Gotha, 1998.

Broecker, W. S., and T. H. Peng, *Tracers in the Sea*, Lamont-Doherty Geol. Observ. of Columbia Univ., Palisades, N. Y., 1982.

Broecker, W. S., and T. H. Peng, The role of $CaCO_3$ compensation in the glacial to interglacial atmospheric CO_2 change, *Glob. Biogeochem. Cycles*, 1, 15–29, 1987.

Broecker, W. S., E. Clark, D. C. McCorkle, T.-H. Peng, I. Hajdas, and G. Bonani, Evidence for a reduction in the carbonate ion content of the deep sea during the course of the Holocene, *Paleoceanography*, 14, 744–752, 1999.

Broecker, W. S., J. Lynch-Stieglitz, and E. Clark, What caused the atmosphere's CO_2 content to rise during the last 8000 years?, *Geochem. Geophys. Geosyst.*, 2, 10.1029/2001GC000177, 2001.

Brovkin, V., A. Ganopolski, and Y. Svirezhev, A continuous climate–vegetation classification for use in climate–biosphere studies, *Ecol. Modell.*, 101, 251–261, 1997.

Brovkin, V., A. Ganopolski, M. Claussen, C. Kubatzki, and V. Petoukhov, Modelling climate response to historical land cover change, *Glob. Ecol. Biogeogr.*, 8, 509–517, 1999.

Chapin, F. S., M. S. Bret-Harte, S. E. Hobbie, and H. L. Zhong, Plant functional types as predictors of transient responses of arctic vegetation to global change, *J. Veg. Sci.*, 7, 347–358, 1996.

Cheddadi, R., G. Yu, J. Guiot, S. P. Harrison, and I. C. Prentice, The climate of Europe 6000 years ago, *Clim. Dyn.*, 13, 1–9, 1997.

Claussen, M., and V. Gayler, The greening of Sahara during the mid-Holocene: Results of an interactive atmosphere–biome model, *Glob. Ecol. Biogeogr. Lett.*, 6, 369–377, 1997.

Claussen, M., V. Brovkin, A. Ganopolski, C. Kubatzki, and V. Petoukhov, Modeling global terrestrial vegetation–climate interaction, *Philos. Trans. R. Soc. London, Ser. B*, 353, 53–63, 1998.

Claussen, M., V. Brovkin, A. Ganopolski, C. Kubatzki, V. Petoukhov, and S. Rahmstorf, A new model for climate system analysis: Outline of the model and application to palaeoclimate simulations, *Environ. Model. Assess.*, 4, 209–216, 1999a.

Claussen, M., C. Kubatzki, V. Brovkin, A. Ganopolski, P. Hoelzmann, and H.-J. Pachur, Simulation of an abrupt change in Saharan vegetation at the end of the mid-Holocene, *Geophys. Res. Lett.*, 26(14), 2037–2040, 1999b.

Conkright, M. E., S. Levitus, and T. P. Boyer, *World Ocean Atlas 1994*, U.S. Dept. of Commer., NOAA, NESDIS, Washington, D. C., 1994.

Cox, P., R. Betts, C. Jones, S. Spall, and I. Totterdell, Acceleration of global warming due to carbon-cycle feedbacks in a coupled climate model, *Nature*, 408, 184–187, 2000.

Crowley, T. J., Causes of climate change over the past 1000 years, *Science*, 289, 270–277, 2000.

Cramer, W., et al., Global response of terrestrial ecosystem structure and function to CO_2 and climate change: Results from six dynamic global vegetation models, *Global Change Biol.*, 7, 357–373, 2001.

Crucifix M., M.-F. Loutre, P. Tulkens, T. Fichefet, and A. Berger, Climate evolution during the Holocene: A study with an Earth system model of intermediate complexity, *Clim. Dyn.*, 19, 43–60, 10.1007/S00382-001-0208-6, 2002.

deMenocal, P. B., J. Ortiz, T. Guilderson, J. Adkins, M. Sarnthein, L. Baker, and M. Yarusinski, Abrupt onset and termination of the African Humid Period: Rapid climate response to gradual insolation forcing, *Quat. Sci. Rev.*, 19, 347–361, 2000.

den Elzen, M., A. Beusen, and J. Rothmans, Modelling global biogeochemical cycles: An integrated assessment approach, *RIVM Rep. 461502007*, 104 pp., RIVM, Bilthoven, 1995.

Dickinson, R. E., A. Henderson-Sellers, and P. J. Kennedy, Biosphere–atmosphere transfer scheme (BATS) version 1e as coupled to the NCAR community climate model, *NCAR Tech. Note TN-387+STR*, 72 pp., NCAR, Boulder, Colo., 1993.

Dufresne J.-L., P. Friedlingstein, M. Berthelot, L. Bopp, P. Ciais, L. Fairhead, H. LeTreut, and P. Monfray, On the magnitude of positive feedback between future climate change and the carbon cycle, *Geophys. Res. Lett.*, 29(10), doi:10.1029/2001GL013777, 2002.

Foley, J., The sensitivity of the terrestrial biosphere to climatic change: A simulation of the middle Holocene, *Glob. Biogeochem. Cycles*, 8, 505–525, 1994.

Foley, J., J. E. Kutzbach, M. T. Coe, and S. Levis, Feedbacks between climate and boreal forests during the Holocene epoch, *Nature*, 371, 52–54, 1994.

Francois, L. M., Y. Godderis, P. Warnant, G. Ramstein, N. de Noblet, and S. Lorenz, Carbon stocks and isotopic budgets of the terrestrial biosphere at mid-Holocene and last glacial maximum times, *Chem. Geol.*, 159, 163–189, 1999.

Ganopolski, A., C. Kubatzki, M. Claussen, V. Brovkin, and V. Petoukhov, The influence of vegetation–atmosphere–ocean interaction on climate during the mid-Holocene, *Science*, 280, 1916–1919, 1998.

Ganopolski, A., V. Petoukhov, S. Rahmstorf, V. Brovkin, M. Claussen, A. Eliseev, and C. Kubatzki, CLIMBER-2: A climate system model of intermediate complexity, part 2, Validation and sensitivity tests, *Clim. Dyn.*, 17, 735–751, 2001.

Grootes, P. M., M. Stuiver, J. W. C. White, S. Johnsen, and J. Jouzel, Comparison of oxygen isotope records from the GISP2 and GRIP Greenland ice cores, *Nature*, 366, 552–554, 1993.

Haxeltine, A., and I. C. Prentice, BIOME3: An equilibrium terrestrial biosphere model based on ecophysiological constraints, resource availability and competition among plant functional types, *Glob. Biogeochem. Cycles*, 10, 693–709, 1996.

Hewitt, C. D., and J. F. B. Mitchell, GCM simulation of the climate of 6 kyr BP: Mean changes and interdecadal variability, *J. Clim.*, 9, 3505–3529, 1996.

Hoelzmann, P., D. Jolly, S. P. Harrison, F. Laarif, R. Bonnefille, and H.-J. Pachur, Mid-Holocene land-surface conditions in northern Africa and the Arabian Peninsula: A data set for the analysis of biogeophysical feedbacks in the climate system, *Glob. Biogeochem. Cycles*, 12, 35–52, 1998.

Holdridge, L. R., Determination of world plant formation from simple climate data, *Science*, 105, 367–368, 1947.

Indermühle, A., et al., Holocene carbon cycle dynamics based on CO_2 trapped in ice at Taylor Dome, Antarctica, *Nature*, 398, 121–126, 1999.

Jolly, D., S. P. Harrison, B. Damnati, and R. Bonnefille, Simulated climate and biomes of Africa during the late quaternary: Comparison with pollen and lake status data, *Quat. Sci. Rev.*, 17, 629–657, 1998.

Jouzel, J., C. Lorius, J. R. Petit, C. Genthon, N. I. Barkov, V. M. Kotlyakov, and V. M. Petrov, Vostok ice core: Continuous isotope temperature record over the last climatic cycle (160,000 years), *Nature*, 329, 403–408, 1987.

Kubatzki, C., M. Montoya, S. Rahmstorf, A. Ganopolski, and M. Claussen, Comparison of a coupled global model of intermediate complexity and an AOGCM for the last interglacial, *Clim. Dyn.*, 2001.

Kutzbach, J. E., G. Bonan, J. Foley, and S. P. Harrison, Vegetation and soil feedbacks on the response of the African monsoon to orbital forcing in the early to middle Holocene, *Nature*, 384, 623–626, 1996.

Leemans, R., and W. P. Cramer, The IIASA database for mean monthly values of temperature, precipitation and cloudiness on a global terrestrial grid, *Res. Rep. RR-91-18*, Int. Inst. for Appl. Syst. Anal., Laxenburg, Austria, 1991.

Levis, S., J. A. Foley, V. Brovkin, and D. Pollard, On the stability of the high-latitude climate–vegetation system in a coupled atmosphere–biosphere model, *Glob. Ecol. Biogeogr.*, 8, 489–500, 1999.

Lieth, H., Modeling the primary productivity of the world, in *Primary Productivity of the Biosphere*, edited by H. Lieth and R. H. Whittaker, pp. 237–263, Springer-Verlag, New York, 1975.

Marchal, O., T. F. Stocker, and F. Joos, A latitude-depth, circulation-biogeochemical ocean model for paleoclimate studies: Model development and sensitivities, *Tellus*, 50B, 290–316, 1998.

MacDonald, G. M., et al., Eurasian treeline change linked to the North Atlantic, *Quat. Res.*, 53, 302–311, 2000.

Martin, J. H., G. A. Knauer, D. M. Karl, and W. W. Broenkow, VERTEX: Carbon cycling in the northeast Pacific, *Deep Sea Res.*, 34, 267–285, 1987.

Milliman, J. D., Production and accumulation of calcium carbonate in the ocean: Budget of a nonsteady state, *Glob. Biogeochem. Cycles*, 7, 927–957, 1993.

Millero, F. J., Thermodynamics of the carbon dioxide system in the oceans, *Geochim. Cosmochim. Acta*, 59, 661–677, 1995.

Olson, J., J. A. Watts, and L. J. Allison, Major world ecosystem complexes ranked by carbon in live vegetation: A database, *CDIAC Numer. Data Collect., NDP-017*, 164 pp., Oak Ridge Natl. Lab., Oak Ridge, Tenn., 1985.

Otterman, J., M.-D. Chou, and A. Arking, Effects of nontropical forest cover on climate, *J. Clim. Appl. Meteorol.*, 23, 762–767, 1984.

Petoukhov, V., A. Ganopolski, V. Brovkin, M. Claussen, A. Eliseev, C. Kubatzki, and S. Rahmstorf, CLIMBER-2: A climate system model of intermediate complexity, *Clim. Dyn.*, 16, 1–17, 2000.

Pollard, D., J. C. Bergengren, L. M. Stillwell-Soller, B. Felzer, and S. L. Thompson, Climate simulation for 10,000 and 6,000 years BP using the GENESIS global climate model, *Paleoclimates*, 2, 183–218, 1998.

Post, W. M., A. W. King, and S. D. Wullschleger, Historical variations in terrestrial biospheric carbon cycle, *Glob. Biogeochem. Cycles*, 11, 99–109, 1997.

Prentice, I. C., W. Cramer, S. P. Harrison, R. Leemans, R. A. Monserud, and A. M. Solomon, A global biome model based on plant physiology and dominance, soil properties and climate, *J. Biogeogr.*, 19, 117–134, 1992.

Prentice, I. C., and D. Jolly, Mid-Holocene and glacial-maximum vegetation geography of the northern continents and Africa, *J. Biogeogr.*, 27, 507–519, 2000.

Rau, G. H., T. Takahashi, and D. J. D. Marais, Latitudinal variations in planktonic $\delta^{13}C$: Implications for CO_2 and productivity in past oceans, *Nature*, 341, 516–518, 1989.

Schimel, D. S., B. H. Braswell, E. A. Holland, R. McKeown, D. S. Ojima, T. H. Painter, W. J. Parton, and A. R. Towsend, Climatic, edaphic, and biotic control over storage and turnover of carbon in soil, *Glob. Biogeochem. Cycles*, 8, 279–293, 1994.

Shaffer, G., Biogeochemical cycling in the global ocean, 2, New production, Redfield ratios, and remineralization in the organic pump, *J. Geophys. Res.*, 101, 3723–3745, 1996.

Shaffer, G., J. Bendtsen, and O. Ulloa, Fractionation during remineralization of organic matter in the ocean, *Deep Sea Res.*, 46, 185–204, 1999.

Siegenthaler, U., Carbon dioxide: Its natural cycle and anthropogenic perturbation, in *The Role of Air–Sea Exchange in Geochemical Cycling*, edited by P. Buat-Ménard, pp. 209–247, D. Reidel, Norwell, Mass., 1986.

Six, K. D., and E. Maier-Reimer, Effects of plankton dynamics on seasonal carbon fluxes in an ocean general circulation model, *Glob. Biogeochem. Cycles*, 10, 559–583, 1996.

Svirezhev, Y., Simplest dynamic models of the global vegetation pattern, *Ecol. Modell.*, 124, 131–144, 1999.

Tarasov, P. E., et al., Present day and mid-Holocene biomes reconstructed from pollen and plant macrofossil data from the former Soviet Union and Mongolia, *J. Biogeogr.*, 25, 1029–1053, 1998.

TEMPO, Potential role of vegetation feedback in the climate sensitivity of high-latitude regions: A case study at 6000 years B.P., *Glob. Biogeochem. Cycles*, 10, 727–736, 1996.

Texier, D., N. deNoblet, P. S. Harrison, A. Haxeltine, D. Jolly, S. Joussaume, F. Laarif, I. C. Prentice, and P. Tarasov, Quantifying the role of biosphere–atmosphere feedbacks in climate change: Coupled model simulations for 6000 years BP and comparison with palaeodata for northern Eurasia and Africa, *Clim. Dyn.*, 13, 865–882, 1997.

Velichko, A. A., A. A. Andreev, and V. A. Klimanov, Climate and vegetation dynamics in the tundra and forest zone during the Late Glacial and Holocene, *Quat. Int.*, 41/42, 71–96, 1997.

Woodward, F. I., *Climate and Plant Distribution*, 174 pp., Cambridge Univ. Press, New York, 1987.

Yamanaka, Y., and E. Tajika, The role of the vertical fluxes of particulate organic matter and calcite in the oceanic carbon cycle: Studies using an ocean biogeochemical general circulation model, *Glob. Biogeochem. Cycles*, 10, 361–382, 1996.

———————————

A. Andreev, Forschungsstelle Potsdam, Alfred-Wegener-Institut für Polar- und Meeresforschung, Telegrafenberg A43, D-14473, Potsdam, Germany. (aandreev@awi-potsdam.de)

J. Bendtsen, Danish Center for Earth System Science, Niels Bohr Institute for Astronomy, Physics and Geophysics, Juliane Maries vej 30, DK-2100, Copenhagen, Denmark. (jb@dcess.ku.dk)

V. Brovkin, M. Claussen, A. Ganopolski, C. Kubatzki, and V. Petoukhov, Potsdam-Institut für Klimafolgenforschung, Postfach 601203, D-14412, Potsdam, Germany. (victor@pik-potsdam.de; claussen@pik-potsdam.de; andrey@pik-potsdam.de; kubi@pik-potsdam.de; petukhov@pik-potsdam.de)
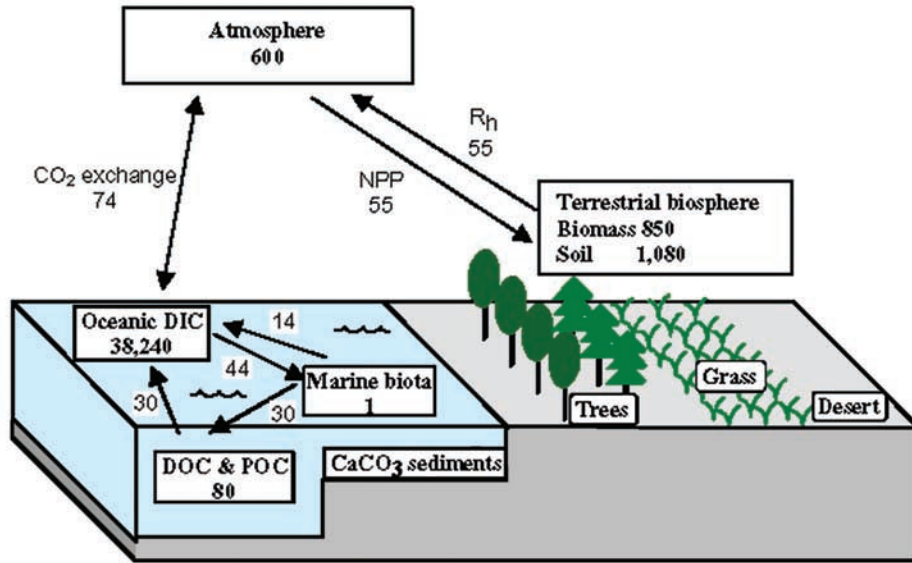
Figure 6. Scheme of the global carbon cycle in CLIMBER-2, preindustrial steady state. Units are Pg for carbon storages and Pg yr^{-1} for carbon fluxes.
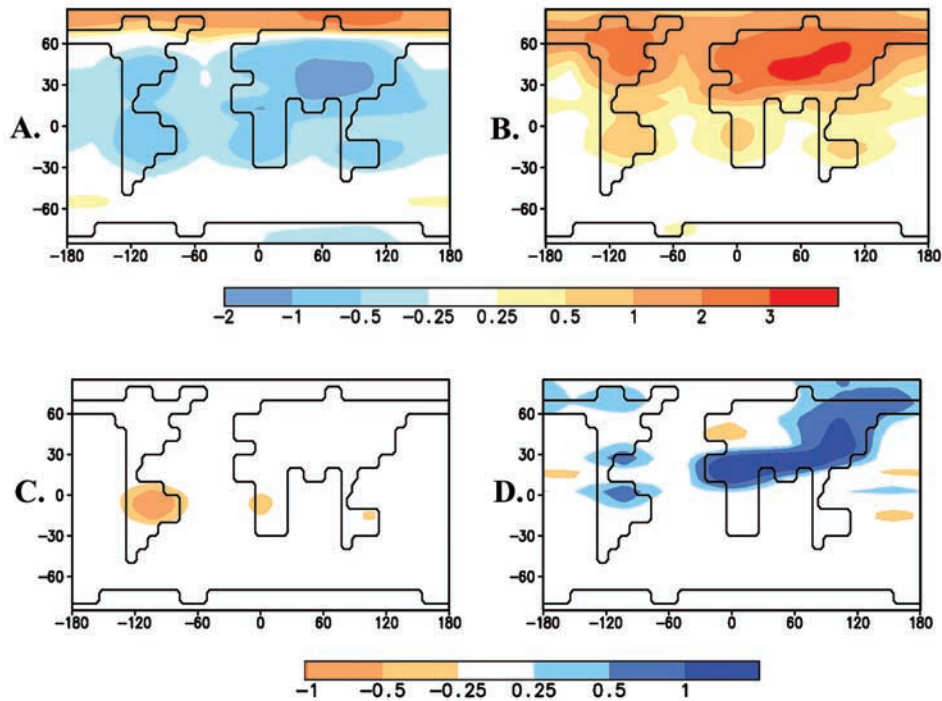

Figure 7. Climatic difference between AOVC-8K and AOVC-0K. (a) and (b) Change in near-surface air temperature (°C) for Northern Hemisphere winter (December–February) and summer (June–August), respectively. (c) and (d) Same as (a) and (b), respectively, but for change in precipitation (mm d^{-1}).
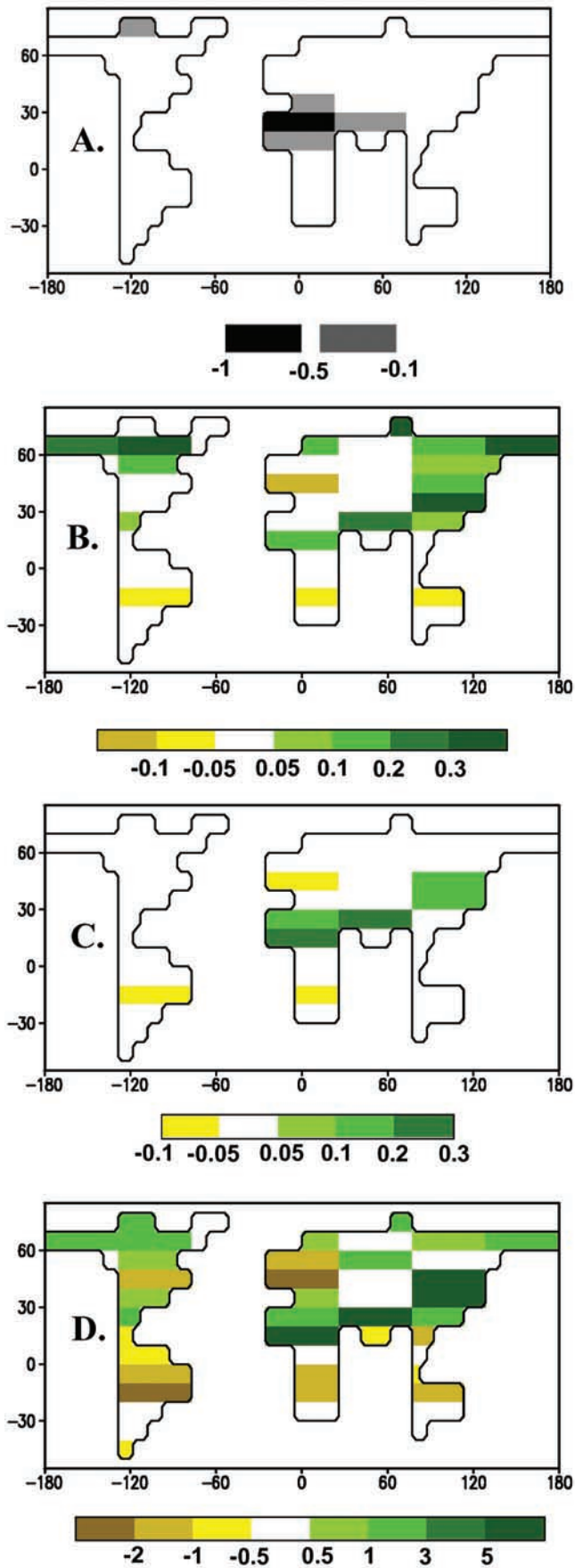
Figure 8. (opposite) Difference in vegetation characteristics between AOVC-8K and AOVC-0K. (a) Desert fraction. (b) Tree fraction. (c) NPP (kgC m^{-2}). (d) Carbon storage (kgC m^{-2}).
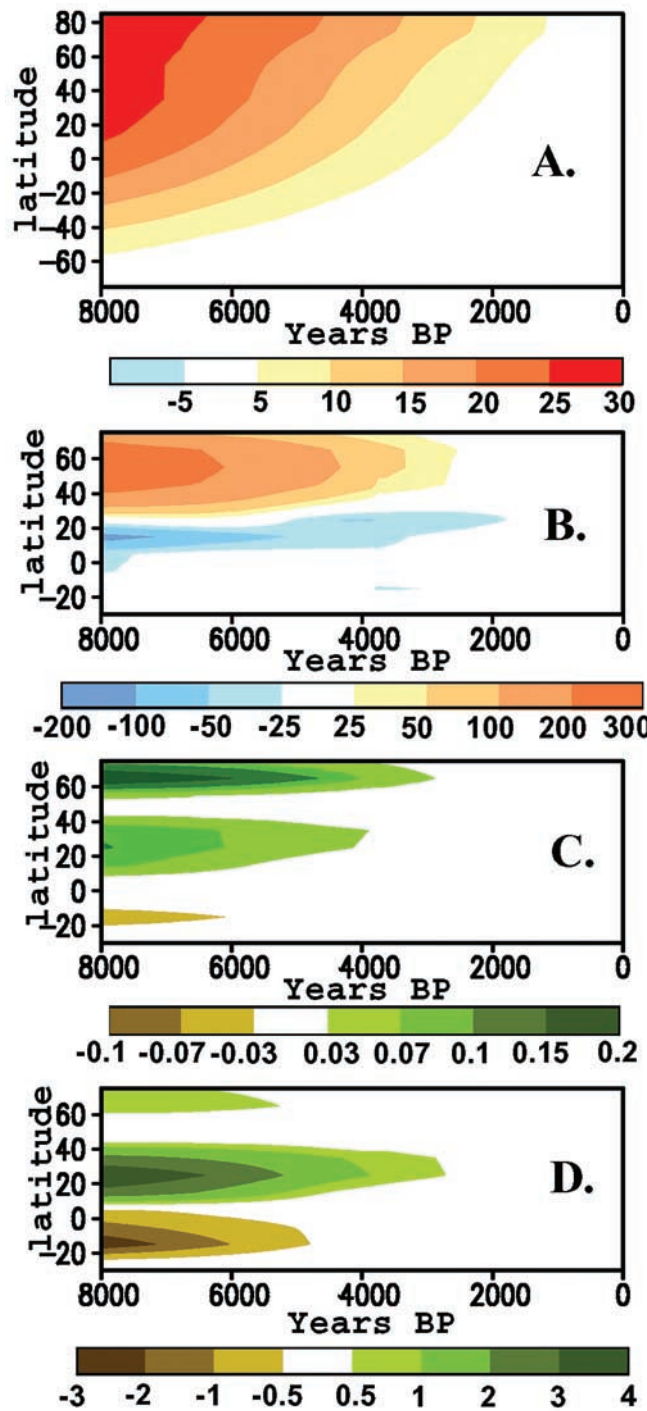
Figure 9. Changes in climate, vegetation, and carbon characteristics, difference between AOVC-T) and (AOVC-0K. (a) Summer irradiation (W m^{-2}), external forcing. (b) Growing degree days (GDD0). (c) Tree fraction. (d) Carbon storage (kgC m^{-2}).